Title	Sensitivity of OWC performance to air compressibility
Author(s)	López, Iván; Carballo, Rodrigo; Taveira-Pinto, Francisco; Iglesias, Gregorio
Publication date	2019-06-20
Original citation	López, I., Carballo, R., Taveira-Pinto, F. and Iglesias, G. (2019) 'Sensitivity of OWC performance to air compressibility', Renewable Energy, 145, pp. 1334-1347. doi: 10.1016/j.renene.2019.06.076
Type of publication	Article (peer-reviewed)
Link to publisher's version	http://www.sciencedirect.com/science/article/pii/S0960148119309048 http://dx.doi.org/10.1016/j.renene.2019.06.076 Access to the full text of the published version may require a subscription.
Rights	© 2019, Elsevier Ltd. All rights reserved. This manuscript version is made available under the CC BY-NC-ND 4.0 license. https://creativecommons.org/licenses/by-nc-nd/4.0/
Embargo information	Access to this article is restricted until 24 months after publication by request of the publisher.
Embargo lift date	2021-06-20
Item downloaded from	http://hdl.handle.net/10468/8154

![UCC logo] University College Cork, Ireland
Coláiste na hOllscoile Corcaigh

1   **Sensitivity of OWC performance to air compressibility**

2   I. López[a,b], R. Carballo[a], F. Taveira-Pinto[b], G. Iglesias[c,d*]

3   *[a] University of Santiago de Compostela, Hydraulic Engineering, Campus Universitario s/n, 27002, Lugo, Spain.*
4   *[b] Faculty of Engineering of the University of Porto, Department of Civil Engineering, Rua Dr. Roberto Frias, s/n, 4200-465,*
5   *Porto, Portugal.*
6   *[c] University College Cork, School of Engineering & MaREI, Environmental Research Institute, Cork, Ireland.*
7   *[d] University of Plymouth, School of Engineering, Marine Building, Drakes Circus, Plymouth, PL4 8AA, United Kingdom.*

8

9   **Abstract**

10   Air compressibility is often neglected in experimental work due to practical difficulties, even though

11   it is known to affect the performance of OWC wave energy converters. The key question, of course, is

12   to what extent. In this work the impact of air compressibility on the capture width ratio is thoroughly

13   quantified by means of a comprehensive experimental campaign, with no fewer than 330 tests

14   encompassing a wide range of wave conditions and levels of turbine-induced damping, and two

15   experimental set-ups: one designed to account for air compressibility, the other to neglect it. This

16   approach is complemented with the use of the RANS-based CFD model OpenFOAM® to calibrate the

17   pressure-vs-flowrate curves, which enables the flowrate to be determined based on the pressure drop

18   measurements from the physical model. We find that the errors that derive from disregarding air

19   compressibility may lead to either under- or over-predictions of power output, and are highly

20   dependent on the operating conditions, more specifically the wave conditions (sea state) and turbine-

21   induced damping.

22   **Keywords**

23   wave energy; wave power; oscillating water column; physical modelling; CFD; capture-width ratio

24   **1. Introduction**

25   Over the last few decades, marine renewable energy has been identified as one of the renewable

26   energy sources of greater potential, theoretically, enough to satisfy the global electric energy demand

27   (Taveira-Pinto *et al.*, 2015). Among the different resources that integrate the marine renewables

28   (waves, currents, tides, wind, thermal resources and salinity gradients), wave energy stands out by its

---

* Corresponding author
  e-mail address: gregorio.iglesias@ucc.ie

29   high density and well-predictability (Arena *et al.*, 2015; Carballo *et al.*, 2015), its low environmental

30   impact (Iglesias and Carballo, 2014), and an exploitability that fully synergizes with other marine

31   renewable resources, such as offshore wind energy (Pérez-Collazo *et al.*, 2015), what enhances its

32   economic viability (Astariz and Iglesias, 2015). Despite the efforts made to design efficient and

33   reliable wave energy converters (WECs) (e.g., Contestabile *et al.*, 2017; López, M. *et al.*, 2017;

34   Stansby *et al.*, 2015), there is no technology at a commercial stage yet. Hence, technological

35   development is, doubtless, the key parameter for driving wave energy to the position that its potential

36   deserves.

37   Among the different types of technologies developed to harvest wave energy, oscillating water

38   column (OWC) devices (Falcão and Henriques, 2016) hold a prominent role. In fact, there are a

39   number of OWC converters that have reached the stage of full-scale prototypes (e.g., Arena *et al.*,

40   2013; Ibarra-Berastegi *et al.*, 2018). An OWC consists mainly in an air turbine and a hollow chamber,

41   partially submerged into the water and connected to the sea through an opening below the water

42   surface. Wave action produces the oscillation of the water column inside the chamber—giving name

43   to the device—and, subsequently, causes the alternating compression and decompression of the air

44   above the water surface, generating an air flow rate which impulses the turbine coupled to a generator.

45   Due to the bidirectional nature of the flow, a special air turbine design is needed. These self-rectifying

46   turbines can be classified according to their operational principle as reaction or impulse type turbines.

47   The reaction working principle has been applied to axial—the well-known Wells turbines

48   (Raghunathan, 1995), radial (Moisel, Christoph and Carolus, 2014) and mixed-flow (Moisel, C. and

49   Carolus, 2015) turbines. Similarly, both axial (Thakker *et al.*, 2004) and radial (Pereiras *et al.*, 2011)

50   impulse type turbines have been developed. A comprehensive overview on self-rectifying turbines can

51   be found in (Falcão and Gato, 2012).

52   The air pressure oscillations that takes place inside an OWC chamber and the subsequent air

53   flow between the chamber and the atmosphere constitute complex thermodynamic processes that

54   induce time-varying changes in air density. This spring-like effect of the air is known to significantly

55   affect the performance of an OWC converter, as was demonstrated by means of analytical ideal-gas

56   models, first, assuming an isentropic relationship between air pressure and density (Sarmento and

57   Falcão, 1985), and then, more realistically, considering changes in entropy due to viscous losses

58   (Falcão and Justino, 1999). More recently, enhanced models based on the real-gas theory were also

59   developed (Medina-López *et al.*, 2017). However, although constitute an essential step in WEC

60   development, analytical models do not consider important non-linear effects (e.g., wave breaking,

61   viscosity or turbulence). Thus, physical or numerical models are a mandatory step in the design

62   process of any converter. Computational fluid dynamic (CFD) techniques have shown to be capable to

63   model OWC devices while accounting for all these effects (e.g., Elhanafi *et al.*, 2017; Simonetti *et al.*,

64   2018). Nevertheless, even the most advanced numerical models require a proper validation based on

65   physical model tests.

66   In small-scale experimental tests, an appropriate modelling of the spring-like effects of air

67   compressibility in the OWC chamber is not straightforward (Weber, 2007). In fact, to correctly

68   reproduce these thermodynamic effects while assuming fully geometric similarity would require to

69   control the ambient pressure to achieve a pressure ratio between model and prototype equal to the

70   length scale ratio (Falcão and Henriques, 2014; Weber, 2007). As pointed by those authors, a feasible

71   possibility to satisfy the scaling requirements of air compressibility is an appropriate adjustment of the

72   air chamber volume, i.e., to not match full geometric similarity, at least in the aerodynamic domain of

73   the OWC model. This is the methodology followed in the experimental model tests carried out by

74   Sarmento (1993) and very recently by Perez-Collazo *et al*. (2018). However, despite the great amount

75   of works published over the last few years dealing with physical modelling of OWC converters (e.g.,

76   Ning *et al.*, 2016; Vyzikas, Deshoulières, Barton *et al.*, 2017), references where the air compressibility

77   effects are taken into account (if any) are scarcely found (Falcão and Henriques, 2016).

78   In this work, an extensive campaign of physical model tests was carried out in order to offer an

79   in-depth evaluation of the effects of the air compressibility on the performance of an OWC wave

80   energy converter, aiming to fully represent the complex physical relationships which other modelling

81   methodologies may not be able to simulate, i.e., without requiring an analytical simplification of the

82   governing processes. The testing campaign involved 330 tests, resulting from the combination of 55

83   regular wave conditions, three different levels of the turbine-induced damping and two set-up

84   configurations. The associated difficulties related to the consideration of the spring-like effect of the

85   air, required the use of numerical methods for calibrating the pressure-vs-flow-rate curves for the

86   different values of the turbine-induced damping. For this purpose, the open-source CFD code

87   OpenFOAM® was used as a complementary tool.

88   This paper is structured as follows. In Section 2, the materials and methods used to investigate

89   the effects of the air compressibility on the performance of the OWC are detailed. First, the physical

90   model campaign and its theorical basis are presented. Second, the numerical model and its

91 characteristics (governing equations, computational domain, mesh and testing programme) are

92 described. Last, the procedures to calculate the capture width ratio of the OWC are established. The

93 results of the investigation are presented in Section 3, focusing on three main aspects: the validation

94 of the numerical model; the pressure-vs-flow-rate curves of the orifices; and the analysis of the

95 sensitivity of the OWC performance to air compressibility. Finally, conclusions are drawn in

96 Section 4.

97 **2. Materials and methods**

98 2.1. Physical modelling

99 When designing a small-scale model of a wave energy converter—as in many other hydraulic

100 applications in which free surface flows are involved—the Froude dynamic similitude criterion must

101 be met (Hughes, 1993), i.e., equal Froude numbers in model and prototype. The Froude number (Fr)

102 is defined as the ratio between the inertia (F_i) and gravity forces (F_g):

$$Fr = \frac{F_i}{F_g} = \frac{v^2}{g\,L} \ , \tag{1}$$

104 where v is a characteristic velocity; g is the gravitational acceleration; and L is a characteristic length

105 of the system.

106   In OWC systems, however, the air compression forces also play an important role. In analogy to

107 the formulation of the Froude number, a non-dimensional number to characterise the compression

108 forces can be formulated (Weber, 2007) as the ratio of the inertia forces (F_i) to the air compression

109 forces (F_c):

$$\frac{F_i}{F_c} = \frac{\rho v^2}{p_0 \gamma} \ , \tag{2}$$

111 where ρ is the fluid density; p_0 is the initial air pressure; and γ is the isentropic exponent. The

112 simultaneous satisfaction of Eqs. (1) and (2) is far from straightforward and often impractical—it

113 would require alterations of the fluid density or the control of the atmospheric pressure. The solution

114 to overcome this (Falcão and Henriques, 2014) is to scale the air chamber volume according to:

$$\frac{V_m}{V_p} = \frac{n_m}{n_p} \varepsilon^2 \delta^{-1} \ , \tag{3}$$

116 where the subscripts m and p refer to model scale and prototype, respectively; V is the air volume of

117 the OWC chamber at still water level; n is the polytropic exponent of the turbine; ε is the length scale

118 ratio (L_m/L_p); and δ is the water density ratio (ρ_m/ρ_p).

119   In sum, an OWC model must ensure that the Froude similitude criterion is met in the

120   hydrodynamic domain (taking into account the maximum elevation that could be achieved by the free

121   surface oscillations) where, in addition, perfect geometric similarity between model and prototype is

122   required (Sheng, Wanan *et al.*, 2014); and a distorted air chamber (in the aerodynamic domain) with a

123   volume that satisfies Eq.(3).
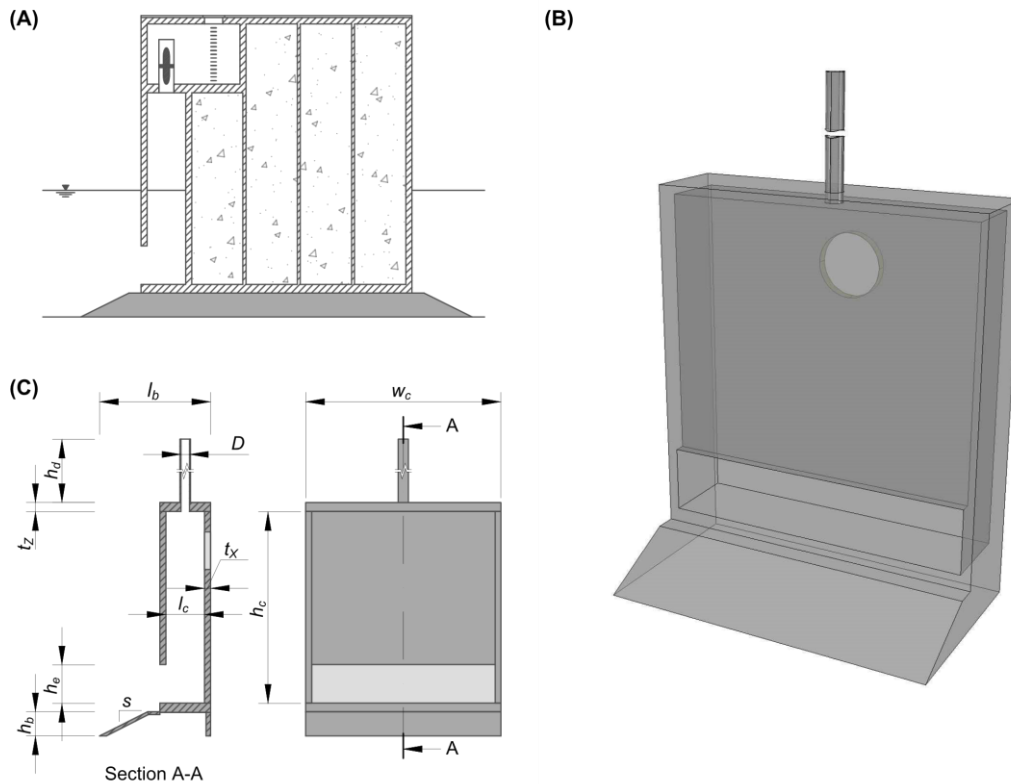
124

125   Figure 1. Schematic of (A) a breakwater-integrated OWC, and 3D perspective (B) and views (C) of the
126   model OWC.

127   The tested OWC model was designed following this methodology. It corresponds to a 1:25

128   small-scale model of a regular design of breakwater-integrated OWC (Figure 1). A summary of the

129   main dimensions of the model is presented in Table 1. It constitutes a 2D model in which the extra air

130   chamber volume, needed to take into account the air compressibility effects, was achieved by

131   connecting the chamber to an air reservoir of appropriate volume. This solution was successfully

132   applied to other fixed-structure OWC devices (Sarmento, 1993). In addition, using an air reservoir

133   rather than a reshaped air chamber enables to assess the effects of the air compressibility on the

134   performance of the OWC with one sole model, by connecting and disconnecting the air reservoir.

5

Table 1. Dimensions of the geometrical parameters of the OWC model

Geometrical parameter	Symbol	Model dimensions
Chamber height	h_c	63.6 cm
Chamber length (in the wave direction)	l_c	12.8 cm
Chamber width (transverse to wave direction)	w_c	65.0 cm
Entrance height	h_e	12.8 cm
Vertical walls thickness	t_Z	2.0 cm
Horizontal walls thickness	t_X	2.8 cm
Orifice diameter	D	variable
Duct height	h_d	$25D$
Bedding height	h_b	8.0 cm
Bedding length	l_b	20.0 cm
Bedding slope	s	1:2

To simulate the turbine-induced damping—a critical variable in the performance of an OWC wave energy converter (López, I. *et al.*, 2014; Sheng, W. and Lewis, 2018)—an orifice was used, which emulates the quadratic pressure-versus-flow-rate relationship of a self-rectifying impulse turbine. In physical model tests, where the turbine can hardly be simulated by a small-scale turbine, using an orifice is a well-established method, in particular when dealing with scale factors below 1:10 (Falcão and Henriques, 2014), although it has also been applied in large-scale experiments (Viviano *et al.*, 2016). Three different values of the turbine-induced damping were used by varying the orifice diameter (D = 28, 31 and 39 mm). These three orifice diameters correspond, approximately, to an area of 0.8%, 1.0% and 1.5% of the plan area of the chamber, respectively; values which are in consonance with previous works (López, I. *et al.*, 2015).

The polytropic exponent of a turbine is related to the turbine efficiency (η) by (e.g., Dixon and Hall, 2014):

$$\eta = \frac{1-\left(p_2/p_1\right)^{1-1/n}}{1-\left(p_2/p_1\right)^{(\gamma-1)/\gamma}} \ , \tag{4}$$

where p_1 and p_2 are the pressures at the inlet and outlet of the turbine, respectively; and the isentropic exponent takes the value of $\gamma = 1.4$ for air. Therefore, the polytropic exponent is a function of the turbine efficiency and the pressure ratio (p_2/p_1). Falcão and Henriques (2014) have shown that the polytropic exponent is approximately constant with respect to the pressure ratio and varies depending on the turbine efficiency between $n = 1$ for the case in which no work is done by the turbine ($\eta = 0$) and $n = 1.4$ for a perfectly efficient turbine ($\eta = 1$). Thus, in the case of a turbine simulated by an orifice the polytropic exponent is $n = 1$. For a state-of-the-art full-size turbine, with an average efficiency of about $\eta = 0.6$, the polytropic exponent is approximately $n = 1.2$ (Falcão and Henriques, 2016). Taking into account these values ($n_m = 1$ and $n_p = 1.2$) together with the dimensions of the

158   OWC to be tested (Table 1), and considering a water density ratio for wave flume testing of $\delta = 0.98$,

159   the air volume of the chamber at 1:25 scale should be, applying Eq.(3), $V_m = 538.4$ dm^3. After

160   subtracting the air volume already contained inside the model chamber (25.2 dm^3) and the air volume

161   contained inside the duct that connects the chamber and the reservoir (18.2 dm^3), the air volume that

162   the reservoir has to supply is equal to 495 dm^3. In the present application, an iron reservoir was used

163   (Figure 2), partially filled with water to remove the volume in excess of the desired one. Care must be

164   taken when designing and constructing the reservoir, as it must resist the pressures generated by the

165   OWC model without becoming deformed, which if happened would introduce undesired effects into

166   the system; similarly, the duct diameter should not be too small.
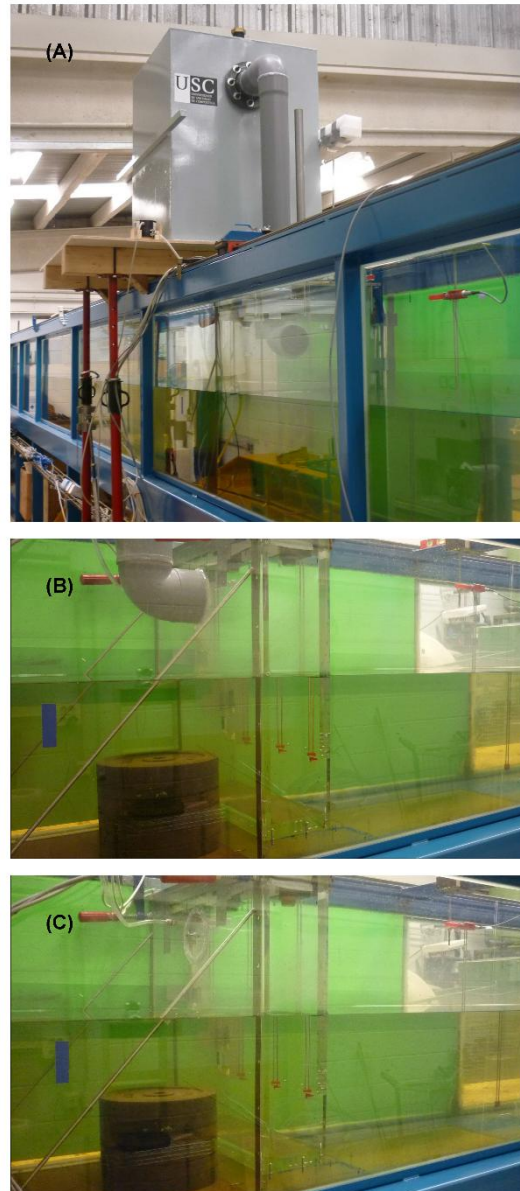
Figure 2. Photographs of (A) a general view of the air reservoir and its connection duct; (B) a detailed view of the connection of the duct to the OWC chamber; and (C) detail of the incompressible set-up without air reservoir.

2.1.1. Experimental testing programme and set-up

In order to thoroughly characterise the performance of the OWC, a total of 55 regular wave conditions were tested, resulting from the combination of five wave heights (H), from $H = 0.02$ m to $H = 0.10$ m, in increments of 0.02 m (from $H = 0.5$ m to $H = 2.5$ m, in prototype dimensions) and eleven wave periods (T), from $T = 1.0$ s to $T = 3.0$ s, in increments of 0.2 s (from $T = 5.0$ s to $T = 15.0$ s, in prototype dimensions). The water depth (h) was set to 0.42 m ($h = 10.5$ m, in prototype dimensions). The 55 wave conditions were tested for the three aforementioned orifice diameters ($D = 28$, 31 and 39

8

178   mm), representative of three different values of the turbine-induced damping. In addition, tests were

179   carried out under two different set-ups: (i) taking into account the air compressibility effects by

180   scaling the chamber air volume proportionally to the square of the scale factor, Eq.(3), (i.e.,

181   connecting the air chamber to the air reservoir); and (ii) assuming air incompressibility at model scale

182   by scaling the chamber air volume with the cube of the scale factor (i.e., disconnecting the air

183   reservoir). In total, the experimental campaign comprised 330 tests.

184   Tests were carried out in the wave flume of the University of Santiago de Compostela, Spain.

185   The flume is 20 m long, 0.95 m high and 0.65 m wide. A piston-type paddle, equipped with an active

186   wave absorption system, *DHI AWACS* (Schäffer and Jakobsen, 2003), that prevents re-reflections of

187   incoming waves, was used for wave generation. The experimental set-up is presented in Figure 3. The

188   OWC model was located at 10.30 m from the paddle, with the air reservoir placed at the rear top of

189   the chamber. Free surface elevation was measured using nine *DHI-202* resistance wave gauges (WGs)

190   distributed along the flume (Figure 3). The measurements of the gauges enabled the monitoring of the

191   incident waves (WG1), the analysis of the incident and reflected waves fields (WG2-5), the

192   verification the waves approaching the model (WG6), and the verification of the absence of transverse

193   waves (WG7-9). Additionally, two *Omega-LVU31* ultrasonic level sensors (US1 and US2) were

194   placed inside the chamber to record the oscillations of the water column. Both types of level sensors,

195   resistance wave gauges and ultrasonic level sensors, have resolutions below 1 mm with an accuracy of

196   millimetres. Finally, the pressure drop between the interior of the chamber and the atmosphere was

197   measured by means of a *GE-Druck-LPM5480* differential pressure sensor (PS), with a range of

198   ±2000 Pa and accuracy of ±0.25% of full scale. The sampling frequency of all the measurement

199   instrumentation was 20 Hz.
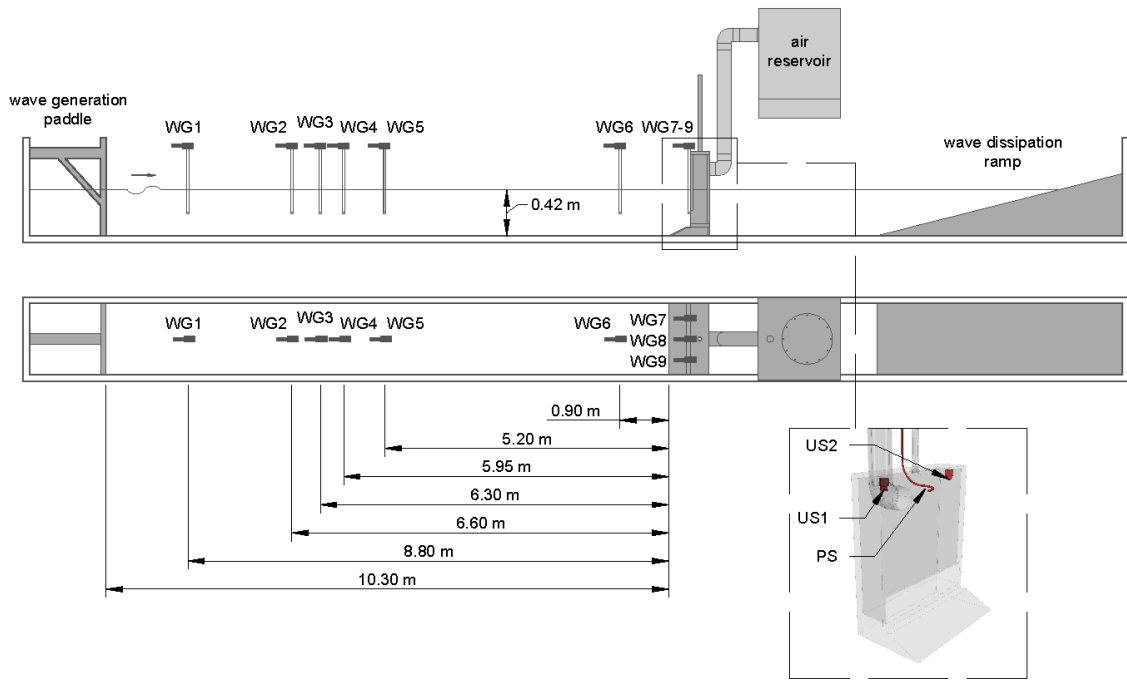
Figure 3. Experimental set-up.

The main caveat when considering air compressibility is the measurement of the air flow rate that, after taking into account the air compressibility, cannot be directly calculated from the motions of the free surface within the chamber. The first attempt was to use an air flow rate meter—hence the use of the duct. Nevertheless, the operational conditions are very demanding (bidirectional flow of relatively high frequency, variable range and high accuracy requirements) and the checked solutions did not show a successful performance. The most common alternative is the calibration of the orifice in order to obtain the relation between the pressure drop and the circulating air flow rate (Sarmento, 1993; Sheng, W. *et al.*, 2013). In this case, the calibration was accomplished through numerical modelling.

Given the small values of the pressure drop ratio (defined as the ratio between the pressure drop through the orifice and the absolute pressure on the inlet side) achieved in the model tests, the expansibility factor of air (Y), which corrects for expansion effects when a compressible fluid passes through an orifice, would become very close to unity, $Y > 0.99$ (Reader-Harris, 2015), which means that the calibration of the orifice remains constant regardless of the air compressibility. This fact enables an incompressible numerical model to be used to calibrate the orifice. Once calibrated, the obtained curves allowed the air flow rate to be computed in the physical model directly from the pressure drop measurements.

219　2.2.　Numerical modelling

220　The open-source computational fluid dynamics (CFD) package OpenFOAM® (version 4.1) was used

221　for modelling the OWC. It is a bundle of different C++ libraries capable of solving a wide variety of

222　continuum mechanics problems (Jasak *et al.*, 2007). Among the different solvers included in the

223　OpenFOAM® package, for solving the motions of the interface between two incompressible phases

224　the *interFoam* solver was used. OpenFOAM® has been successfully used and validated to deal with

225　OWC modelling, both to analyse the hydrodynamics of the device (Vyzikas, Deshoulières, Giroux *et*

226　*al.*, 2017) and to optimise the geometry and the turbine-induced damping (Simonetti *et al.*, 2017).

227　*2.2.1. Governing equations*

228　The numerical model solves the Reynolds averaged Navier–Stokes (RANS) equations, which describe

229　the flow motion of a fluid. The RANS equations consist of a mass conservation equation, Eq.(5), and

230　a momentum conservation equation, Eq.(6), expressed as:

231
$$\frac{\partial u_i}{\partial x_i} = 0 \ , \tag{5}$$

232
$$\frac{\partial \rho u_i}{\partial t} + u_j \frac{\partial \rho u_i}{\partial x_j} = -\frac{\partial p^*}{\partial x_i} - g_i X_j \frac{\partial \rho}{\partial x_i} + \frac{\partial}{\partial x_j}\left[\mu_{eff} \frac{\partial u_i}{\partial x_j} \right] + f_{\sigma,i} \ , \tag{6}$$

233　where i, j = 1, 2, 3 denote the Cartesian components of the three-dimensional vectors or tensors; u_i is

234　the ith component of the velocity vector; ρ is the density of the fluid; p^* is the pseudo-dynamic

235　pressure; g_i is ith component of the gravitational acceleration; X_i is the position vector; μ_{eff} is the

236　effective dynamic viscosity ($\mu_{eff} = \mu + \rho v_t$, where μ is the molecular dynamic viscosity and v_t is the

237　turbulent kinematic viscosity given by the turbulence model); finally, $f_{\sigma,i}$ is the ith component of the

238　surface tension tensor term.

239　　　As mentioned above, a turbulence model which provide a value for the turbulent kinematic

240　viscosity is needed for the closure of the equations. In this case, the k-ω SST turbulence model was

241　used. This model combines the best features of the k-ϵ and k-ω models showing good results in

242　simulating OWC devices (Iturrioz *et al.*, 2015), other wave energy conversion technologies (Schmitt

243　and Elsaesser, 2015) and also wave-structure interaction problems in coastal engineering (Higuera *et*

244　*al.*, 2013).

245　　　The movements of the interface between the air and water phases was tracked by the volume-of-

246　fluid (VOF) method (Hirt and Nichols, 1981). This method uses a phase-fraction function (α) defined

247　as the fraction of the cell volume filled with water: for a cell full of water the phase-fraction function

11

248   takes a value of $\alpha = 1$, for a cell full of air $\alpha = 0$, and $0 < \alpha < 1$ for an interface cell which contains

249   both air and water. The tracking of the free surface movements is modelled by means of the following

250   advection equation:

251
$$\frac{\partial \alpha}{\partial t} + \frac{\partial u_i \alpha}{\partial x_i} + \frac{\partial u_{c,i} \alpha (1-\alpha)}{\partial x_i} = 0 \; , \tag{7}$$

252   where the last term on the left-hand-side is an artificial compression term (Deshpande *et al.*, 2012)

253   introduced to achieve a sharper interface, being $u_{c,i}$ the artificial compression velocity.

254   For wave generation and absorption, the relaxation technique included in the *waves2Foam*

255   toolbox was used (Jacobsen *et al.*, 2012). This technique forms part of the internal wave generation

256   methods, in which waves are generated within a region defined inside the numerical domain. In

257   addition, the relaxation zones enable passive wave absorption to avoid reflection of waves into the

258   computational domain. Thus, wave generation and absorption are accomplished by modifying the

259   velocity, pressure and phase-fraction function inside the relaxation zone following:

260
$$\phi = \alpha_R \phi_{computed} + (1 - \alpha_R) \phi_{target} \; , \tag{8}$$

261   where ϕ represents any flow variable in the relaxation zone for which the solution will be a weighted

262   combination of the numerical model solution and a target or desired solution forced over the

263   relaxation zone; and α_R is the relaxation function, defined as (Jacobsen *et al.*, 2012):

264
$$\alpha_R (\chi_R) = 1 - \frac{\exp\left(\chi_R^{3.5}\right) - 1}{\exp(1) - 1} \quad \text{for} \quad \chi_R \in [0,1] \; , \tag{9}$$

265   where χ_R is the coordinate along the *x*-axis scaled to the length of the relaxation zone.

266   *2.2.2. Computational domain*

267   The numerical model faithfully reproduces the experimental set-up, with the differences inherent to

268   numerical wave generation through relaxation zones, that is, the numerical wave flume incorporates

269   an upstream extra section—the relaxation zone region (Figure 4)—where waves are generated and

270   absorbed, emulating the wave generation and absorption system of the experimental wave flume.

271   There is no outlet relaxation zone as no waves go beyond the OWC model; for the same reason, the

272   numerical flume ends just behind the OWC. Furthermore, the numerical model takes advantage of a

273   symmetry boundary condition to only simulate one half of the flume, which brings important

274   computational cost savings. The length of the computational domain from the end of the relaxation

275   zone (where wave propagation starts) to the front wall of the OWC model was set, as in the

276   experimental set-up, to 10.30 m.
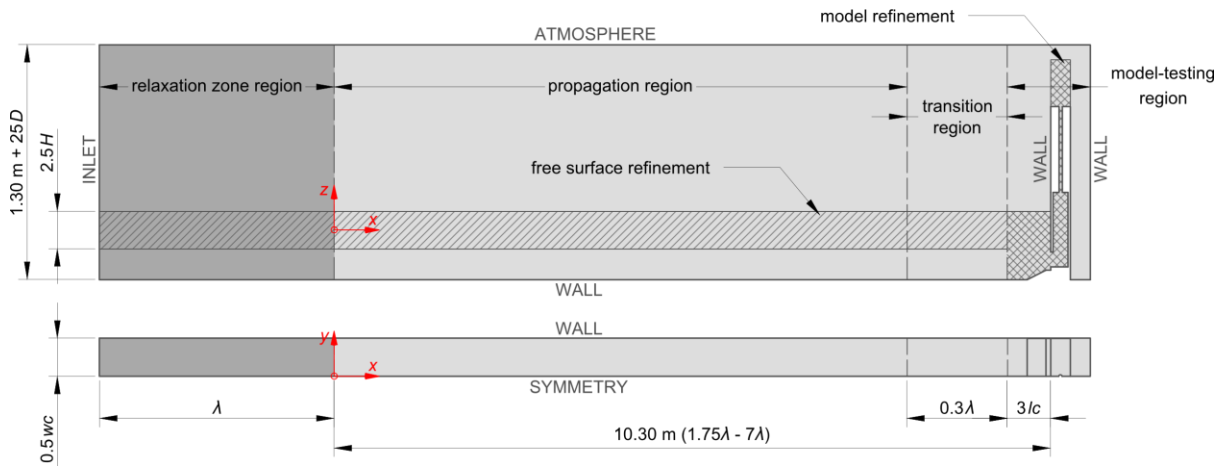
Figure 4. Computational domain. The boundary conditions are indicated in capital letters.

The computational domain was spatially discretised using the *snappyHexMesh* utility, a mesh generator which, starting from a simple background mesh that is iteratively refined and morphed, outputs a hexahedral mesh conformed to a given geometric surface. Attending to the characteristics of the mesh, four main regions can be distinguished (Figure 4): the relaxation region, the propagation region, the transition region and the model-testing region. In the three first regions (relaxation, propagation and transition regions) the mesh is parameterised based on the wave conditions to be simulated, i.e., the cell size varies depending on the wave height and the wave period. The characteristics of the model-testing zone, however, remains constant despite changes in the wave conditions. With this methodology of different mesh regions, a uniform grid with a cell aspect ratio equal to one—optimum for the performance of the *snappyHexMesh* utility—can be generated in the location of the OWC model, without affecting the mesh of the remaining domain. The computational mesh is presented in Figure 5.
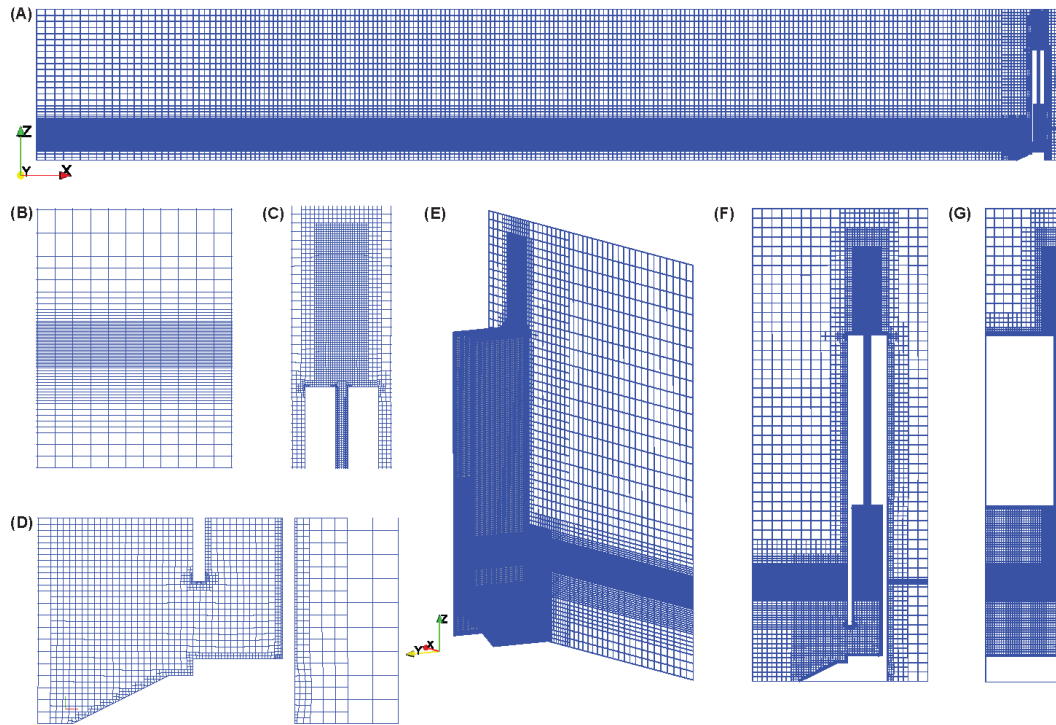
Figure 5. Computational mesh: (A) general view of the numerical wave flume; (B) detail of the mesh around the free surface; (C) detail of the mesh around the outlet of the orifice; (D) detail of the mesh around the entrance of the chamber; (E) perspective view zoomed in the model-testing region; (F) slice orthogonal to the y-axis at $y = 0$ (symmetry boundary); and (G) slice orthogonal to the x-axis at $x = 10.384$ m (x-coordinate of the centre of the orifice).

In the propagation region, the mesh is uniform along the x-axis, with a cell size that ensures 50 cells per wavelength, a value already used in similar applications (Vanneste and Troch, 2015). As mentioned above, the length of this region is constant in order to faithfully reproduce the experimental set-up; therefore, following previous works (López, I. et al., 2014), a non-uniform mesh was set along the z-axis, with a finer sub-mesh around the free surface. The minimum cell size was set to $\Delta z = 0.005$ m for $H = 0.04\text{-}0.06$ m, and to $\Delta z = 0.010$ m for $H = 0.08\text{-}0.10$ m, to match the ratio $H/\Delta z \geq 8$ (Simonetti et al., 2017). For the smallest waves ($H = 0.02$ m) it was found that a ratio $H/\Delta z \geq 2$ is enough (Vanneste and Troch, 2015), so the cell size was set to $\Delta z = 0.005$ m. As the distance to the free surface increases, the cell size is doubled successively, maintaining the cell size constant during, at least, three layers. The growth is faster towards the air domain where a maximum cell size of $\Delta z = 0.08$ m was set. Those settings, both on the x- and z-axis, were maintained in the relaxation region, whose total length was established to one wavelength, a solution successfully employed in upstream relaxation zones (e.g., Hu et al., 2016; Simonetti et al., 2017). The z-axis settings of the propagation region were maintained, again, in the transition region. However, along the x-axis a growing rate was established to ensure a smooth transition from the cell size in the

14

312 propagation region to that in the model-testing region. The total length of the transition region was set

313 to 0.3 wavelength. In these three regions, the cell size in the y-axis was set to $\Delta y = 0.04$ m, resulting in

314 8 cells along this axis; which is enough as no meaningful flow is expected in this direction.

315   Finally, in the un-parametrized mesh of the model-testing region a base cell size of

316 $\Delta x = \Delta y = \Delta z = 0.04$ m was used. This base size was refined progressively in all directions (using up

317 to five refinement levels) in the proximity of the OWC model contours to obtain a mesh that better fits

318 the model. A minimum of two cell layers of each size was established to improve the mesh

319 smoothness. The area in the interior of the chamber and at the front of the OWC model was refined to

320 $\Delta x = \Delta y = \Delta z = 0.01$ m and at the free surface to $\Delta x = \Delta y = \Delta z = 0.005$ m. In addition, an extra

321 refinement was made in the orifice duct and its inlet and outlet area matching that of the free surface.

322   The boundary conditions were set to *wall* for the bottom, left-side, and rear boundaries, as well

323 as for all the boundaries of the OWC model (Figure 4). The *wall* boundary condition implies no-slip

324 condition for velocity, zero-gradient conditions for pressure and phase-fraction function, and special

325 wall functions for k and ω according to the k-ω SST turbulence model. At the *inlet*, special wave

326 generating functions were implemented for velocity and phase-fraction (Jacobsen *et al.*, 2012),

327 whereas zero-gradient conditions were set for pressure. At the *atmosphere*, the pressure was set to a

328 fixed total value equal to zero, the velocity to a *pressureInletOutletVelocity* condition in which a zero-

329 gradient condition is applied for outflow, and for inflow the velocity is calculated from the flux

330 through the boundary; the phase-fraction function was set to an *inletOutlet* condition, which switches

331 between zero-gradient for outflow, and a fixed value set to zero (air), for the case of return flow.

332 Finally, the right-side of the computational domain was set to a symmetry boundary.

333 *2.2.3. Numerical testing programme*

334 The aim of the numerical tests is the calibration of the three orifices that emulate the turbines. Given

335 that the pressure-vs-flow-rate depends on the characteristics of the orifice, and not on the wave

336 conditions that forced them (Sheng, W., Thiebaut *et al.*, 2013), calibrating the orifices for the whole

337 set of wave conditions is not necessary. In any case, a heterogeneous selection of nine wave

338 conditions were tested to prove the previous statement, covering five different wave periods and five

339 wave heights (Table 2).

340

Table 2. Wave conditions included in the numerical testing programme.

Wave condition	Model dimensions		Prototype dimensions	
	T	H	T	H
#1	1.20 s	0.06 m	6 s	1.5 m
#2	1.60 s	0.02 m	8 s	0.5 m
#3	1.60 s	0.04 m	8 s	1.0 m
#4	1.60 s	0.06 m	8 s	1.5 m
#5	1.60 s	0.08 m	8 s	2.0 m
#6	1.60 s	0.10 m	8 s	2.5 m
#7	2.00 s	0.06 m	10 s	1.5 m
#8	2.40 s	0.06 m	12 s	1.5 m
#9	2.80 s	0.06 m	14 s	1.5 m

341   However, the first milestone when dealing with numerical modelling is the validation. In this

342   case, it was carried out through the comparison between the experimental measurements (from the

343   incompressible set-up) and the numerical model data. The heterogeneity of the wave conditions

344   selected for the numerical programme ensure a meaningful validation without reproducing the whole

345   experimental set. In order to validate the model, both the pressure drop between the interior of the

346   chamber and the atmosphere, and the oscillations of the water column were measured. Additionally,

347   the free surface elevations along the flume were measured at the same positions defined in the

348   experimental set-up (Figure 3). The flow rate through the orifice was also measured for calibrating the

349   orifice.

350   The performance of the numerical model for each wave condition was evaluated on the basis of

351   the correlation coefficient and the normalised root mean square error (Appendix A).

352   2.3. Data analysis

353   Once the numerical model was validated, the next step was to obtain the calibration curves of the

354   three orifices. For each numerical test, the data points of pressure drop versus flow rate were fitted

355   with a parabolic curve centred at the origin (López, I. *et al.*, 2016) that can be expressed, for

356   exhalation stage ($\Delta p > 0$) by:

$$\Delta p = B_{exh} Q^2 \ , \tag{10}$$

358   and for inhalation stage ($\Delta p < 0$) by:

$$\Delta p = -\left(B_{inh}\right)Q^2 \ , \tag{11}$$

360   where Δp is the pressure drop between the interior of the chamber and the atmosphere, Q is the flow

361   rate and B is a damping parameter. The damping parameters for each orifice were calculated as the

362   average of the nine damping parameter values obtained from the wave conditions tested. Given the

363   closeness between the inhalation and exhalation values, a representative damping parameter (B_r) was

364   subsequently calculated as the average of the values of both stages. Finally, based on previous works

365   (López, I. *et al.*, 2014), a dimensionless damping coefficient was defined as:

$$B^* = \frac{\Delta p^{1/2}}{Q} \frac{A_c}{\rho_a^{1/2}} = B_r^{1/2} \frac{A_c}{\rho_a^{1/2}} \;, \tag{12}$$

367   where A_c is the plant area of the OWC chamber ($A_c = l_c \times w_c$); and ρ_a is the air density. The damping

368   coefficient is, therefore, a dimensionless parameter that characterises the turbine-induced damping.

369   From the numerical obtained damping parameters of the three orifices and the experimental

370   pressure drop data, the instantaneous flow rate for each one of the 330 experimental tests was

371   calculated following:

$$Q = \mathrm{sgn}(\Delta p) \left(\frac{|\Delta p|}{B_r} \right)^{1/2} . \tag{13}$$

373   Known the instantaneous pressure drop and the flow rate, the mean pneumatic power is given

374   by:

$$P_p = \frac{1}{t_{max}} \int_0^{t_{max}} \Delta p Q \, dt . \tag{14}$$

376   Once the pneumatic power is calculated, the second key variable to evaluate the performance of

377   an OWC is the wave power. First, the incident and reflected wave fields were obtained by means of a

378   reflection analysis carried out using the Mansard and Funke (Mansard and Funke, 1980) method

379   modified by Baquerizo (1995). Second, based on the incident wave spectrum the mean power of the

380   incident waves per unit width of converter was computed as:

$$P_w = \rho_w g \int_0^\infty S(\omega) c_g(\omega) d\omega \;, \tag{15}$$

382   where ρ_w is the water density; $S(\omega)$ is the spectral density; and c_g is the group velocity, defined as:

$$c_g = \frac{1}{2} \left(1 + \frac{2kh}{\sinh(2kh)} \right) \frac{\omega}{k} \;, \tag{16}$$

384   where k is the wave number; h is the water depth; and ω is the angular frequency, which is obtained

385   from the dispersion relationship:

$$\omega^2 = gk \tanh(kh) . \tag{17}$$

387   Finally, the capture width ratio (also known as relative capture width) of the OWC, i.e., the

388   efficiency in transforming the power of the incoming waves into pneumatic power, is defined as:

$$C_{WR} = \frac{P_p}{w_c P_w} . \tag{18}$$

390   where w_c is the width of the OWC chamber (Figure 1).

3. Results and discussion

3.1. Numerical model validation

The results of the numerical model validation for the pressure drop and the free surface elevation inside the OWC chamber are summarised in Table 3. Excellent agreement is found, with an average value of the correlation coefficient for the entire validation set close to unity and a NRMSE well below 10%, both for pressure drop ($R = 0.992$, NRMSE = 7.29%) and free surface elevation ($R = 0.986$, NRMSE = 5.90%). Although a slight performance decrease is observed when the orifice diameter increases, the results are good and consistent for the three orifice diameters tested. Comparing the results between the pressure drop and free surface elevation signals, a better agreement is found for the latter, as shows the lower value of the NRMSE: 7.29% for pressure drop vs 5.90% for the free surface elevation. The magnitude of the errors is of the same order of those achieved in previous OWC numerical models, either using an OpenFOAM® code (e.g., Simonetti *et al.*, 2017) or different commercial codes (e.g., López, I. *et al.*, 2014).

Table 3. Results of the numerical model validation based on the comparison between the experimental and numerical signals of pressure drop (Δp) and free surface elevation inside the OWC chamber (η_{OWC}).

D (mm)	Δp				η_{OWC}			
	R		NRMSE		R		NRMSE	
	average	*s*	*average*	*s*	*average*	*s*	*average*	*s*
28	0.9922	0.0044	0.0680	0.0186	0.9878	0.0044	0.0547	0.0131
31	0.9956	0.0073	0.0645	0.0204	0.9867	0.0050	0.0592	0.0117
39	0.9878	0.0097	0.0861	0.0316	0.9844	0.0113	0.0632	0.0159
	0.9919	**0.0079**	**0.0729**	**0.0252**	**0.9863**	**0.0074**	**0.0590**	**0.0136**

The excellent agreement is qualitatively illustrated in Figure 6, which shows the superposition of the pressure drop and free surface elevation inside the chamber from both models, physical and numerical. For clarity, only 10 s of simulation are presented. The agreement found is, again, very good. Thus, both the amplitude and the period of the pressure drop and the water column oscillations are well reproduced by the numerical model for the three orifice diameters tested. As was previously found by means of the NRMSE, the performance of the model is shown to better reproduce the free surface elevations of the water column than the pressure drop, with the amplitude of the latter slightly overpredicted. It should also be noted, that the phase between both signals is well reproduced by the numerical model too, which is paramount for a correct reproduction of the pressure-vs-flow-rate curves.

18

416
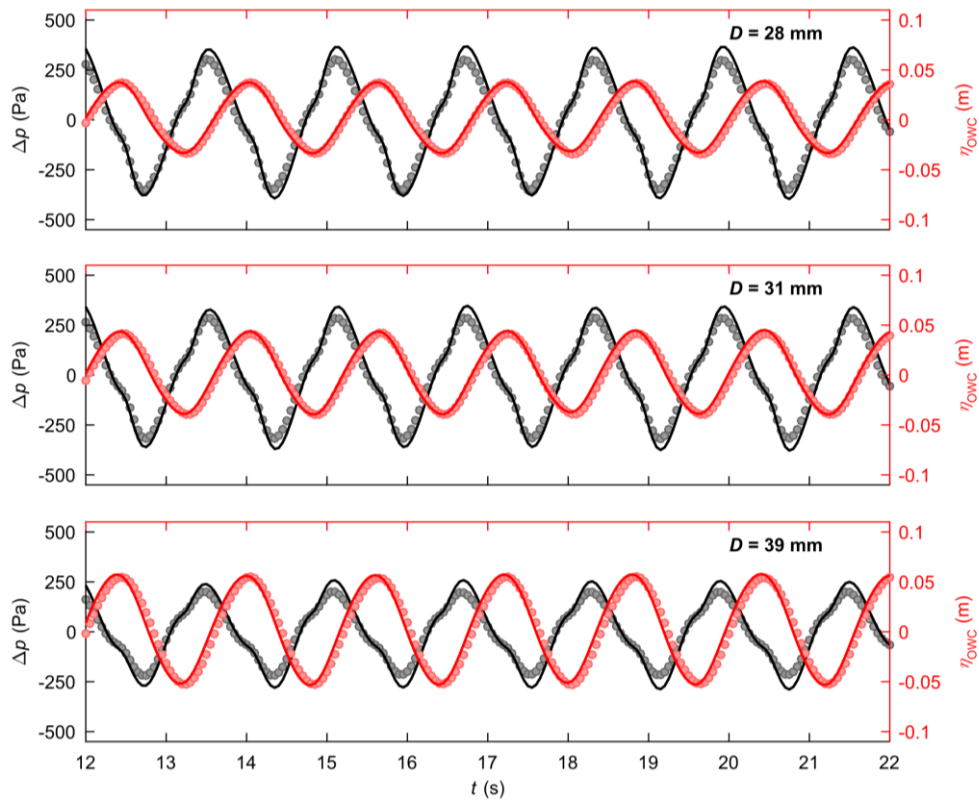
Figure 6. Pressure drop (black) and free surface elevations of the water column inside the chamber (red) corresponding to a wave condition with $H = 0.06$ m and $T = 1.6$ s, for the three orifice diameters tested (— numerical model; ○ physical model).
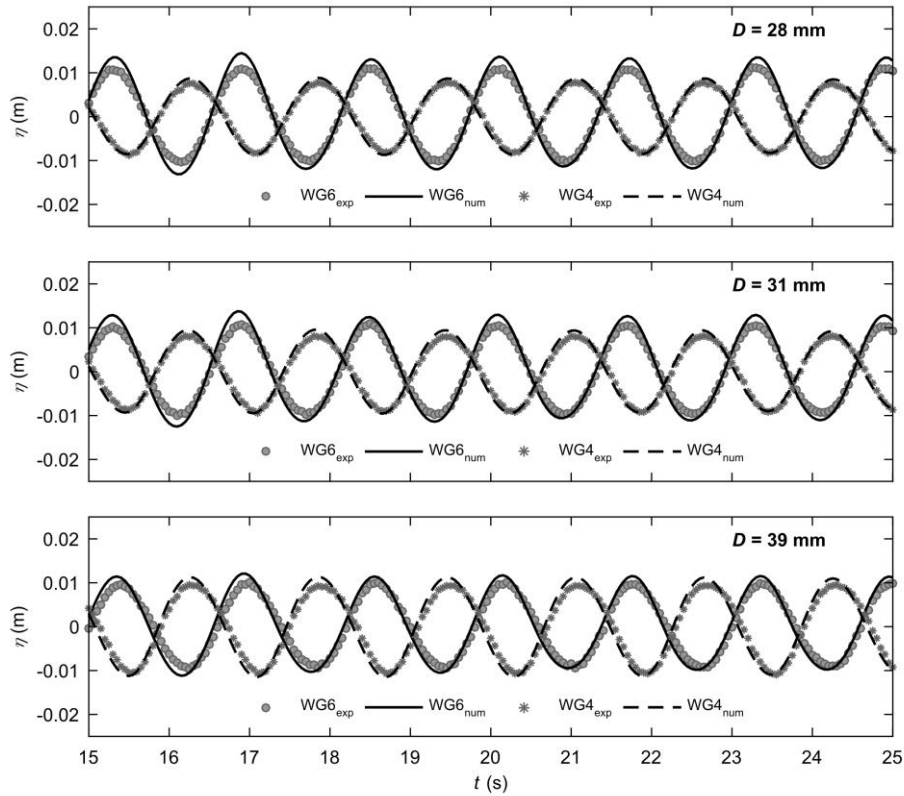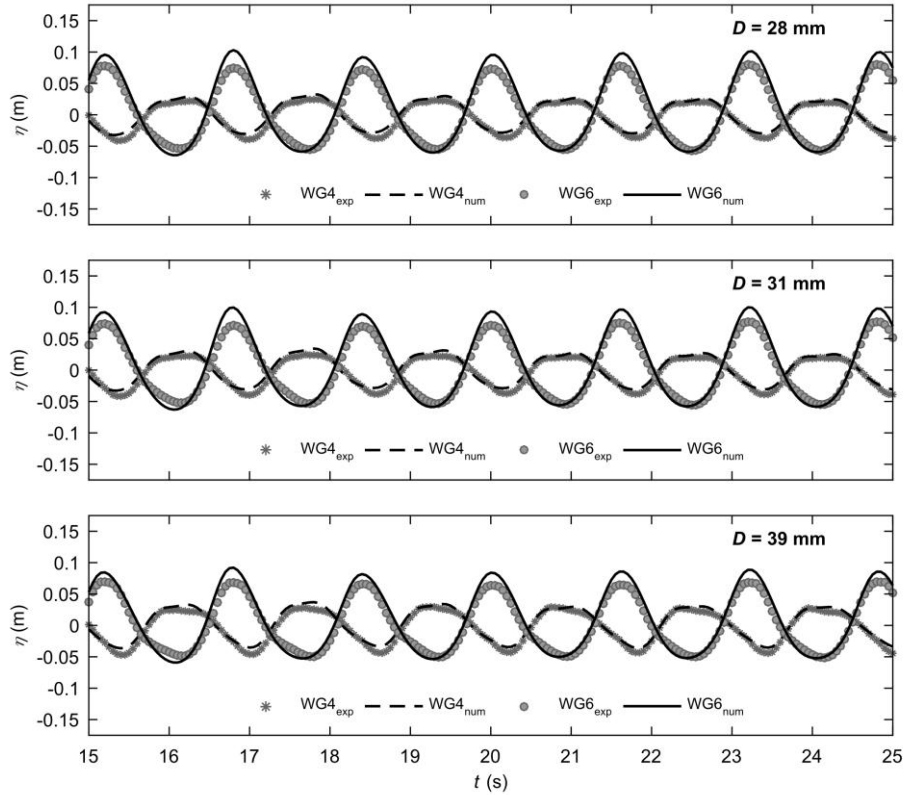
Furthermore, the time series of free surface elevations obtained from the physical and numerical models at two positions, one at the middle of the flume and the other in front of the OWC model, i.e., at WG4 and WG6 (Figure 3), are also compared, first, in Figure 7, for the wave condition with the smallest wave height ($H = 0.02$ m; $T = 1.6$ s), and second, in Figure 8, for the wave condition with the largest wave height ($H = 0.10$ m; $T = 1.6$ s). The agreement found for both wave conditions is, as in the previous validation cases, excellent. Both the wave height and period are well reproduced by the numerical model all along the flume, as show the matching between the signals measured and computed at WG4 and WG6 positions. In general, the agreement is slightly higher for the smaller waves, which is probably due to their being better represented through linear theory. Interestingly, it can be seen that the amplitude of the wave profiles varies depending on the diameter of the orifice considered. This is due to the different energy absorption of the OWC for each orifice and, consequently, to the variation in existing reflected waves.

Figure 7. Time series of free surface elevation (η) at WG4 and WG6 positions, corresponding to a wave condition with $H = 0.02$ m and $T = 1.6$ s, for the three orifice diameters tested.

Figure 8. Time series of free surface elevation (η) at WG4 and WG6 positions, corresponding to a wave condition with $H = 0.10$ m and $T = 1.6$ s, for the three orifice diameters tested.

20

438   The quantitative results of the validation of the free surface elevation at WG4 and WG6 positions

439   are presented in Table 4. The average value of the correlation coefficient is, for the two wave

440   conditions and at both positions, close to unity ($R > 0.98$). Similarly, the NRMSE is well below 10%,

441   both for the smallest and the largest wave, although it is slightly higher in the case of the latter.

442   Table 4. Results of the numerical model validation based on the comparison between the experimental
443   and numerical signals of free surface elevation at two positions along the flume (η_{WG4} and η_{WG6}), for two
444   different wave conditions.

| D (mm) | $H = 0.02$ m, $T = 1.6$ s | | | | $H = 0.10$ m, $T = 1.6$ s | | | |
| | η_{WG4} | | η_{WG6} | | η_{WG4} | | η_{WG6} | |
	R	NRMSE	R	NRMSE	R	NRMSE	R	NRMSE
28	0.9983	0.0635	0.9960	0.0379	0.9952	0.0816	0.9886	0.0806
31	0.9974	0.0665	0.9948	0.0443	0.9967	0.0859	0.9863	0.0835
39	0.9857	0.0718	0.9839	0.0708	0.9950	0.0823	0.9884	0.0776
	0.9938	**0.0673**	**0.9916**	**0.0510**	**0.9956**	**0.0833**	**0.9878**	**0.0806**

445   All in all, the results of the validation process demonstrate that the numerical model

446   implemented accurately reproduces the behaviour of an OWC wave energy converter under different

447   values of the turbine-induced damping.

448   3.2. Orifice calibration curves

449   Once validated, the numerical model was used to extract the pressure-vs-flow-rate curves for the three

450   orifice diameters, corresponding to three different values of the turbine-induced damping. The data

451   points and the parabolic curves which fit them for each one of the orifice diameters are presented in

452   Figure 9. The values of the representative damping parameter for each damping condition are

453   presented in Table 5.
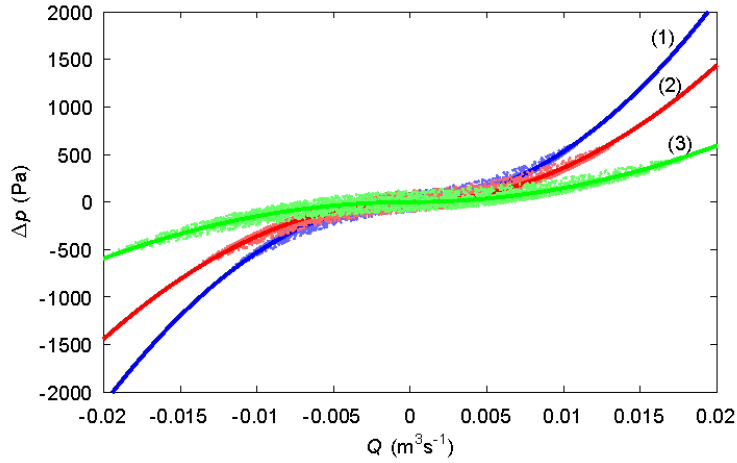
454

458 The agreement between the dataset and the fitted curves is very good, which confirms the

459 quadratic pressure-vs-flow-rate relationship. Furthermore, it indicates that the damping parameters are

460 consistent regardless of the wave height and wave period. This statement is also corroborated by the

461 low values of the standard deviation presented in Table 5. Given the small difference between the

462 inhalation and exhalation values of the damping parameter, the use of an average representative value

463 for both stages (B_r) is justified.

464 Table 5. Inhalation, exhalation and representative values of the damping parameter (B) for the
465 three orifice diameters tested.

D (mm)	B_{inh} (kg/m^7)		B_{exh} (kg/m^7)		B_r (kg/m^7)
	average	*s*	*average*	*s*	*average*
28	5.33×10^6	9.72×10^4	5.27×10^6	8.24×10^4	5.30×10^6
31	3.59×10^6	7.54×10^4	3.59×10^6	6.86×10^4	3.59×10^6
39	1.48×10^6	3.59×10^4	1.48×10^6	3.77×10^4	1.48×10^6

466 Finally, the values of the dimensionless damping coefficient for the three orifice diameters,

467 $D = 28$, 31 and 39 mm, calculated through Eq. (12), are $B^* = 160.49$, 132.18 and 84.85, respectively.

468 3.3. Air compressibility effects

469 The values of the capture width ratio calculated for the 55 wave conditions tested under three

470 damping conditions and two different set-ups, incompressible (assuming full geometric similarity)

471 and compressible (scaling correctly the chamber air volume by enlarging it through an air reservoir),

472 are presented in Figure 10. The effects of the air compressibility can be easily evaluated by comparing

22

473   the first and second column of graphs, or directly in the graphs of the third column which show the

474   relative difference in the C_{WR} between the incompressible and compressible set-up.
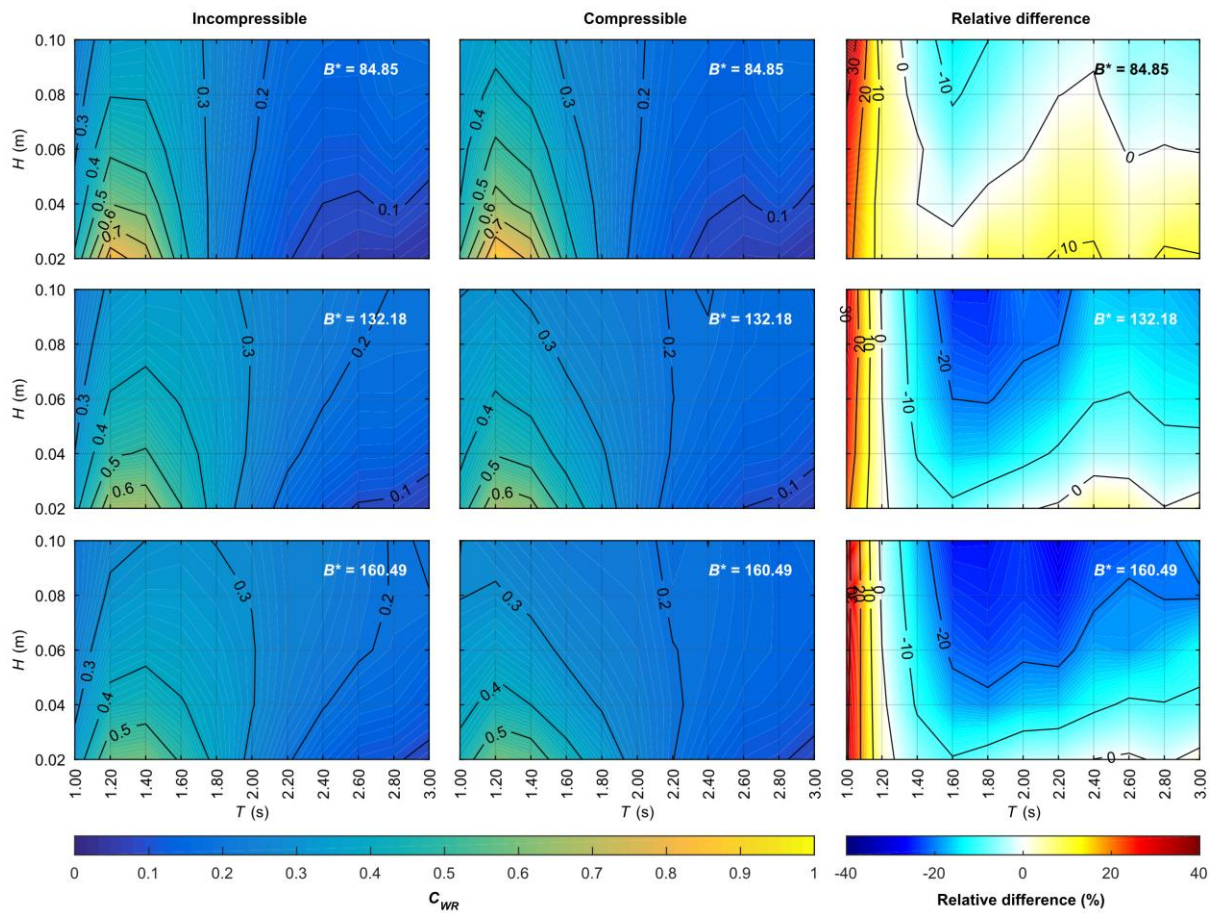
475

476   Figure 10. In the first and second column of graphs, variation of the capture width ratio (C_{WR}) with the
477   wave height (H) and the wave period (T) under the three damping conditions tested, for the
478   incompressible (first column) and compressible (second column) set-ups; in the third column, variation
479   of the relative difference between the capture width ratio of the compressible set-up with respect to the
480   incompressible one.

481   First, it could be interesting to analyse separately each set-up, incompressible and compressible.

482   In the incompressible set-up (Figure 10 – left column), the results point that, for the OWC model

483   tested, there is a resonant period (an optimum period which maximises the C_{WR}) in the vicinity of

484    $T = 1.20\text{-}1.40$ s, that substantially improves the C_{WR}; and the maximum performance is achieved for

485   the lower wave heights. Second, the influence of the wave height is much more complex: for wave

486   periods close to the resonant, the higher the wave height, the lower the C_{WR}; on the contrary, for larger

487   periods far away from the resonant (around $T = 3.0$ s), the higher the wave height, the greater the C_{WR}.

488   For intermediate periods (around $T = 2.0$ s), the influence of the variation in wave height is much

489   lower, producing only slight variations in the C_{WR}. Third, the damping, known to be a critical

23

490　parameter on the performance of an OWC (López, I. *et al.*, 2015), plays also an important role: an

491　appropriate selection can improve the maximum capture width ratio from $C_{WR} < 60\%$ for the higher

492　damping ($B^* = 160.49$) to $C_{WR} > 80\%$ for the lower damping ($B^* = 84.85$). There is not, though, a

493　damping condition that is optimum for every wave condition, it varies depending on the wave height

494　and period combination. All these findings are in accordance with those provided by previous works

495　(e.g., López, I. *et al.*, 2015; Rezanejad *et al.*, 2017), contributing again to validate the methodology

496　followed in this work.

497　　　　Attending to the compressible set-up (Figure 10 – centre column), overall, all the previous

498　results remain valid. This fact gives relevance to the incompressible testing, which constitutes a valid

499　approach to obtain a general view of the performance of an OWC wave energy converter. However, a

500　careful comparative analysis points out subtle differences. In this way, in the incompressible set-up,

501　the resonant period changes depending both on the damping conditions and on the wave height. When

502　the damping coefficient increases, the resonant period changes towards greater wave periods, e.g., for

503　$B^* = 84.85$ and $H = 0.02$ m, the resonant period is $T = 1.20$ s, whereas for $B^* = 160.49$ and $H =$

504　0.02 m, the resonant period increases to $T = 1.40$ s. Moreover, it can be seen that the resonant period

505　also moves to greater values when the wave height increases, e.g., for $H = 0.02$ m and $B^* = 132.18$ the

506　resonant period is $T = 1.40$ s, whereas for $H = 0.10$ m and $B^* = 132.18$, the resonant period increases

507　to $T = 1.60$ s. This behaviour becomes more evident for the greater values of the damping coefficient.

508　In the compressible set-up, however, the resonant period remains constant at the same value

509　($T = 1.20$ s) independently of both the damping conditions and the wave height.

510　　　　More importantly, the capture width ratio is also altered by the air compressibility effects, as

511　indicates the relative difference between the C_{WR} of the compressible set-up with respect to the

512　incompressible one (Figure 10 – right column). The results show that the influence of the air

513　compressibility on the capture width ratio highly depends on the wave conditions. Thus, for the

514　smaller wave periods ($T < 1.20$ s), the air compressibility exerts a positive influence on the C_{WR}, with

515　improvements on the performance of the OWC higher than 30%. On the contrary, for greater periods

516　($T > 1.20$ s), the air compressibility produces a reduction of the C_{WR} up to -28.2%. In addition, the

517　damping plays an important role, mainly for the wave conditions of $T > 1.20$ s: for the greater value of

518　the damping coefficient ($B^* = 160.49$), air compressibility negatively impacts the C_{WR} for practically

519　the whole range of wave heights; nevertheless, for the lower value of the damping coefficient

520　($B^* = 84.85$), the air compressibility effects are positive from the point of view of the C_{WR} for the

521   wave conditions with lower wave heights ($H < 0.06$ m). For these waves with greater period

522   ($T > 1.20$ s), overall, the greater the wave height, the greater the negative impact of the air

523   compressibility effects. This result is related to the findings of Simonetti *et al.*, (2018), who point that

524   scaling effects due to air compressibility become more important as the pressure drop increases (in

525   general, higher wave heights produce greater oscillations of the water column and, therefore, greater

526   pressure differences).

527   Complementarily to the previous analysis, it is also interesting to establish the overall influence

528   of air compressibility, by averaging the capture width ratio over the whole set of wave conditions for

529   both set-ups, incompressible and compressible (Table 6). The relative difference between the global

530   average values of the capture width ratio between the incompressible and compressible set-ups is

531   about 10% for the greater values of the damping coefficient ($B^* = 132.18$ and 160.49), drastically

532   changing for the lower damping condition ($B^* = 84.85$) under which the relative difference is positive

533   and greater than 3%. Therefore, it is shown, again, that the damping plays an important role in the

534   performance of an OWC converter, determining the direction of the overall influence of the air

535   compressibility effects on the capture width ratio. Furthermore, when air compressibility effects are

536   taken into account the optimum damping coefficient (i.e., that which maximises the C_{WR} for the whole

537   set of wave conditions) changes: the optimum damping coefficient for the incompressible set-up is the

538   intermediate one ($B^* = 132.18$), whereas for the compressible set-up is the lowest ($B^* = 84.85$). This

539   is of paramount importance given that a wrong evaluation of the optimum damping could lead to a

540   wrong dimensioning of the turbine (Pereiras *et al.*, 2015).

541   Table 6. Global average values of the capture width ratio (C_{WR}) considering the whole set of
542   wave conditions, for the three values of the damping coefficient.

B^*	C_{WR}		Relative difference (%)
	incompressible set-up	*compressible set-up*	
160.49	0.278	0.250	−9.99
132.18	0.284	0.261	−8.08
84.85	0.256	0.265	+3.58

543   In the recent literature, only a couple of works focused on the effects of the air compressibility

544   on the performance of an OWC considering non-linear effects (i.e., without analytical simplifications

545   of the governing processes), both carried out by numerical modelling (Elhanafi *et al.*, 2017; Simonetti

546   *et al.*, 2018). For the testing conditions (wave height, wave period and damping conditions)

547   considered in these works, overestimations of the OWC performance in the order of 10% was found

548   when air compressibility effects are disregarded. These works, however, only point to a negative

549   impact of the air compressibility, which is probably related to the reduced range of testing conditions

550   considered. In any case, despite the limited conditions tested, Elhanafi *et al.* (2017) highlighted that

551   the overestimation in OWC efficiency is more pronounced for wave periods larger than the resonant,

552   and noted the influence of the damping conditions, results which are in line with those presented in

553   this work. The complex nature of the air compressibility effects on the OWC performance was also

554   pointed out, through an analytical model, by Falcão *et al.* (2014), who emphasise that disregarding air

555   compressibility effects leads to errors which change its sign depending on the wave period.

556   **4.   Conclusions**

557   In this work, the influence of air compressibility on the performance of an OWC wave energy

558   converter was thoroughly evaluated through physical modelling. To take into account the air

559   compressibility, the scaling of the air volume of the OWC chamber was performed according to the

560   square of the length scale ratio ($V \propto \varepsilon^2$) using an air reservoir to provide the additional air volume

561   required. Moreover, an incompressible set-up was also tested by assuming full geometric similarity (

562    $V \propto \varepsilon^3$), i.e., disconnecting the air reservoir. The experimental campaign involved a total of 330 tests,

563   resulting from the combination of 55 wave conditions and three different values of the turbine-

564   induced damping, tested for two different set-ups, compressible and incompressible. The flow rate

565   was calculated from pressure drop data measurements using calibrated pressure-vs-flow-rate curves

566   for each of the three orifices which represent as many damping conditions. The calibration curves

567   were obtained by means of the open source RANS-based CFD model OpenFOAM®, coupled with the

568   *waves2Foam* toolbox for wave generation. The numerical model was successfully validated based on

569   the experimental results (pressure drop and free surface elevation inside the OWC chamber), both

570   quantitatively ($R_{average} > 0.98$, $NRMSE_{average} < 8\%$) and qualitatively (by direct comparison of the

571   measurements from both models).

572   Based on the results of the experimental campaign, the following conclusions may be drawn.

573   First, the incompressible set-up (i.e., full geometric similarity by scaling the air chamber volume to

574   the cube of the length scale ratio) constitutes a useful approach to study an OWC in its early stages of

575   development, for it leads to findings broadly similar to those obtained with the compressible set-up:

576   (i) existence of a resonant period that maximises the capture width ratio (C_{WR}); (ii) significant

577   influence of the damping on the C_{WR}; and (iii) complex influence of the wave height on the C_{WR},

578   mainly governed by the wave period. However, disregarding air compressibility introduces spurious

26

579   variations of the resonant period when testing conditions change and, more importantly, leads to

580   wrong estimates of the capture width ratio. Thus, although using an incompressible set-up could be a

581   valid approach in the early stages of design, it must be avoided when an in-depth analysis of the

582   performance of the OWC is required.

583   Second, the air compressibility effects significantly affect the efficiency of the OWC, altering the

584   C_{WR} with respect to that of the incompressible set-up, approximately, in the range of −30 to 30 per

585   cent, depending, mainly, on the wave conditions. Thus, air compressibility effects are highly

586   influenced by the sea state. In general, disregarding air compressibility leads to underpredictions of

587   the C_{WR} for periods below the resonant period, and to overpredictions for larger periods. Furthermore,

588   it was shown that the damping plays a fundamental role in the performance of an OWC converter,

589   determining the direction and magnitude of the overall influence of the air compressibility effects on

590   the C_{WR}. It was also found that the optimum damping coefficient (critical parameter for dimensioning

591   the turbine) decreases when air compressibility effects are taken into account; it follows that

592   neglecting air compressibility could well lead to suboptimal specifications for the turbine. As a final

593   remark, air compressibility effects are complex and, consequently, do not lend themselves to a

594   simplification in the form of an overall percentage value – the variation of the performance of the

595   OWC over the entire range of operating conditions must be considered.

596   In sum, the spring-like effect of air compressibility in the chamber is important in an OWC wave

597   energy converter. Should this effect be disregarded, significant errors would be introduced in the

598   assessment of the device efficiency, including both under- and over-predictions, depending on the sea

599   state and the turbine-induced damping. In light of these results, it may be concluded that air

600   compressibility must be considered in all but the preliminary stages of design or analysis.

Appendix A. Error estimators

The performance of the numerical model for each wave condition was evaluated on the basis of the correlation coefficient, defined as:

$$R = \frac{s_{xy}}{s_x s_y} \tag{A.1}$$

where s_{xy} represents the covariance between the measurements from the experimental tests and the corresponding values from the numerical model tests; and s_x and s_y represent the sample standard deviation of the experimental and numerical tests, respectively. Additionally, the normalised root mean square error was also calculated as:

$$\text{NRMSE} = \frac{1}{x_{max} - x_{min}} \left[\frac{1}{N} \sum_{i=1}^{N} (x_i - y_i)^2 \right]^{1/2} \tag{A.2}$$

where x_i represents the i-th data element of the measurements from the experimental tests; y_i represents the corresponding value from the numerical model tests; N is the total number of data points; and $x_{max} - x_{min}$ represent the range of the data from the experimental test considered. It is preferred over the average because of the sinusoidal nature of the data (the average is close to zero).

References

Arena, F., Laface, V., Malara, G., Romolo, A., Viviano, A., Fiamma, V., et al., 2015. Wave climate analysis for the design of wave energy harvesters in the Mediterranean Sea. Renew.Energy 77, 125-141. https://doi.org/10.1016/j.renene.2014.12.002.

Arena, F., Romolo, A., Malara, G., Ascanelli, A., 2013. On design and building of a U-OWC wave energy converter in the Mediterranean Sea: a case study. 32nd International Conference on Ocean, Offshore and Arctic Engineering (OMAE) , Nantes, France, pp. V008T09A102. https://doi.org/10.1115/OMAE2013-11593.

Astariz, S., Iglesias, G., 2015. The economics of wave energy: A review. Renew.Sust.Energ.Rev. 45, 397-408. https://doi.org/10.1016/j.rser.2015.01.061.

Baquerizo, A., 1995. Wave reflection at beaches. PhD Thesis, University of Cantabria, Spain.

Carballo, R., Sánchez, M., Ramos, V., Fraguela, J.A., Iglesias, G., 2015. Intra-annual wave resource characterization for energy exploitation: A new decision-aid tool. Energy Conv.Manag. 93, 1-8. https://doi.org/10.1016/j.enconman.2014.12.068.

Contestabile, P., Di Lauro, E., Buccino, M., Vicinanza, D., 2017. Economic Assessment of Overtopping BReakwater for Energy Conversion (OBREC): A Case Study in Western Australia. Sustainability 9 (1), 51. https://doi.org/10.3390/su9010051.

639   Deshpande, S.S., Anumolu, L., Trujillo, M.F., 2012. Evaluating the performance of the two-phase
640   flow solver interFoam. Comput.Sci.Disc. 5 (1), 014016. https://dx.doi.org/10.1088/1749-
641   4699/5/1/014016.

642   Dixon, S.L., Hall, C.A., 2014. Fluid Mechanics and Thermodynamics of Turbomachinery.
643   Butterworth-Heinemann, Boston.

644   Elhanafi, A., Macfarlane, G., Fleming, A., Leong, Z., 2017. Scaling and air compressibility effects on
645   a three-dimensional offshore stationary OWC wave energy converter. Appl.Energy 189, 1-20.
646   https://doi.org/10.1016/j.apenergy.2016.11.095.

647   Falcão, A.F.O., Gato, L.M.C., 2012. 8.05 - Air Turbines. In: A. Sayigh (Ed.), Comprehensive
648   Renewable Energy, Elsevier, Oxford, pp. 111-149. https://dx.doi.org/10.1016/B978-0-08-
649   087872-0.00805-2.

650   Falcão, A.F.O., Henriques, J.C.C., 2014. Model-prototype similarity of oscillating-water-column
651   wave energy converters. Int.J.Mar.Energy 6, 18-34.
652   https://dx.doi.org/10.1016/j.ijome.2014.05.002.

653   Falcão, A.F.O., Henriques, J.C.C., 2016. Oscillating-water-column wave energy converters and air
654   turbines: A review. Renew.Energy 85, 1391-1424.
655   https://dx.doi.org/10.1016/j.renene.2015.07.086.

656   Falcão, A.F.O., Justino, P.A.P., 1999. OWC wave energy devices with air flow control. Ocean Eng.
657   26 (12), 1275-1295. https://doi.org/10.1016/S0029-8018(98)00075-4.

658   Higuera, P., Lara, J.L., Losada, I.J., 2013. Simulating coastal engineering processes with
659   OpenFOAM®. Coast.Eng. 71, 119-134. https://doi.org/10.1016/j.coastaleng.2012.06.002.

660   Hirt, C.W., Nichols, B.D., 1981. Volume of fluid (VOF) method for the dynamics of free boundaries.
661   J.Comput.Phys. 39 (1), 201-225. https://doi.org/10.1016/0021-9991(81)90145-5.

662   Hu, Z.Z., Greaves, D., Raby, A., 2016. Numerical wave tank study of extreme waves and wave-
663   structure interaction using OpenFoam®. Ocean Eng.
664   126, 329-342. https://doi.org/10.1016/j.oceaneng.2016.09.017.

665   Hughes, S.A., 1993. Physical models and laboratory techniques in coastal engineering. World
666   Scientific, Singapore.

667   Ibarra-Berastegi, G., Sáenz, J., Ulazia, A., Serras, P., Esnaola, G., Garcia-Soto, C., 2018. Electricity
668   production, capacity factor, and plant efficiency index at the Mutriku wave farm (2014–2016).
669   Ocean Eng.147, 20-29. https://doi.org/10.1016/j.oceaneng.2017.10.018.

670   Iglesias, G., Carballo, R., 2014. Wave farm impact: The role of farm-to-coast distance. Renew.Energy
671   69, 375-385. https://dx.doi.org/10.1016/j.renene.2014.03.059.

672   Iturrioz, A., Guanche, R., Lara, J.L., Vidal, C., Losada, I.J., 2015. Validation of OpenFOAM® for
673   Oscillating Water Column three-dimensional modeling. Ocean Eng.
674   107, 222-236. https://doi.org/10.1016/j.oceaneng.2015.07.051.

675   Jacobsen, N.G., Fuhrman, D.R., Fredsøe, J., 2012. A wave generation toolbox for the open- source
676   CFD library: OpenFoam®. Int.J.Numer.Methods Fluids 70 (9), 1073-1088.
677   https://doi.org/10.1002/fld.2726.

678   Jasak, H., Jemcov, A., Tukovic, Z., 2007. OpenFOAM: A C++ library for complex physics
679   simulations. International Workshop on Coupled Methods in Numerical Dynamics, Dubrovnik,
680   Croatia, pp. 1-20.

681   López, I., Pereiras, B., Castro, F., Iglesias, G., 2014. Optimisation of turbine-induced damping for an
682   OWC wave energy converter using a RANS–VOF numerical model. Appl.Energy 127, 105-114.
683   https://doi.org/10.1016/j.apenergy.2014.04.020.

684   López, I., Pereiras, B., Castro, F., Iglesias, G., 2015. Performance of OWC wave energy converters:
685   influence of turbine damping and tidal variability. Int.J.Energy Res. 39 (4), 472-483.
686   https://doi.org/10.1002/er.3239.

687   López, I., Pereiras, B., Castro, F., Iglesias, G., 2016. Holistic performance analysis and turbine-
688   induced damping for an OWC wave energy converter. Renew.Energy 85, 1155-1163.
689   https://dx.doi.org/10.1016/j.renene.2015.07.075.

690   López, M., Taveira-Pinto, F., Rosa-Santos, P., 2017. Numerical modelling of the CECO wave energy
691   converter. Renew.Energy 113, 202-210. https://doi.org/10.1016/j.renene.2017.05.066.

692   Mansard, E.P.D., Funke, E.R., 1980. The measurement of incident and reflected spectra using a least
693   squares method. 17th International Conference on Coastal Engineerig, Sydney, Australia, pp.
694   154-172. https://doi.org/10.1061/9780872622647.008.

695   Medina-López, E., Moñino, A., Borthwick, A.G.L., Clavero, M., 2017. Thermodynamics of an OWC
696   containing real gas. Energy 135, 709-717. https://doi.org/10.1016/j.energy.2017.06.164.

697   Moisel, C., Carolus, T.H., 2015. Novel mixed flow air-turbine for bidirectional operation in OWC
698   wave energy converters. 11th European Wave and Tidal Energy Conference (EWTEC), Nantes,
699   France, pp. 1-10.

700   Moisel, C., Carolus, T.H., 2014. Radial lift-based cascade for bi-directional wave energy air-turbines.
701   ASME Turbo Expo 2014: Turbine Technical Conference and Exposition, Düsseldorf, Germany,
702   pp. V02DT42A017. https://dx.doi.org/10.1115/GT2014-25821.

703   Ning, D., Wang, R., Zou, Q., Teng, B., 2016. An experimental investigation of hydrodynamics of a
704   fixed OWC Wave Energy Converter. Appl.Energy 168, 636-648.
705   https://doi.org/10.1016/j.apenergy.2016.01.107.

706   Pereiras, B., Castro, F., el Marjani, A., Rodriguez, M.A., 2011. An improved radial impulse turbine
707   for OWC. Renew. Energy 36 (5), 1477-1484. https://doi.org/10.1016/j.renene.2010.10.013.

708   Pereiras, B., López, I., Castro, F., Iglesias, G., 2015. Non-dimensional analysis for matching an
709   impulse turbine to an OWC (oscillating water column) with an optimum energy transfer. Energy
710   87, 481-489. https://dx.doi.org/10.1016/j.energy.2015.05.018.

711   Pérez-Collazo, C., Greaves, D., Iglesias, G., 2015. A review of combined wave and offshore wind
712   energy. Renew.Sust.Energ.Rev. 42, 141-153. https://dx.doi.org/10.1016/j.rser.2014.09.032.

713   Perez-Collazo, C., Greaves, D., Iglesias, G., 2018. A Novel Hybrid Wind-Wave Energy Converter for
714   Jacket-Frame Substructures. Energies 11 (3) https://doi.org/10.3390/en11030637.

715   Raghunathan, S., 1995. The wells air turbine for wave energy conversion. Prog. Aerospace Sci. 31
716   (4), 335-386. https://doi.org/10.1016/0376-0421(95)00001-F.

717   Reader-Harris, M., 2015. Orifice plates and venturi tubes. Springer International, Cham.

718   Rezanejad, K., Guedes Soares, C., López, I., Carballo, R., 2017. Experimental and numerical
719   investigation of the hydrodynamic performance of an oscillating water column wave energy
720   converter. Renew.Energy 106, 1-16. https://doi.org/10.1016/j.renene.2017.01.003.

721   Sarmento, A., 1993. Model-test optimization of an OWC wave power plant. Int.J.Offshore Polar Eng.
722   3 (1), 66-72.

723   Sarmento, A., Falcão, A.F.O., 1985. Wave generation by an oscillating surface-pressure and its
724   application in wave-energy extraction. J.Fluid Mech. 150, 467-485.
725   https://doi.org/10.1017/S0022112085000234.

726   Schäffer, H.A., Jakobsen, K.P., 2003. Non-linear wave generation and active absorption in wave
727   flumes. Proc.Long Waves Symposium, Thessaloniki, Greece, pp. 69-77.

728   Schmitt, P., Elsaesser, B., 2015. On the use of OpenFOAM to model oscillating wave surge
729   converters. Ocean Eng.
730   108, 98-104. https://doi.org/10.1016/j.oceaneng.2015.07.055.

731   Sheng, W., Alcorn, R., Lewis, A., 2013. On thermodynamics in the primary power conversion of
732   oscillating water column wave energy converters. J.Renew.Sustain.Energy 5 (2), 023105.
733   https://doi.org/10.1063/1.4794750.

734   Sheng, W., Lewis, A., 2018. Power takeoff optimization to maximize wave energy conversions for
735   Oscillating Water Column devices. IEEE J.Ocean.Eng. 43 (1), 36-47.
736   https:10.1109/JOE.2016.2644144.

737   Sheng, W., Thiebaut, F., Babuchon, M., Brooks, J., Lewis, A., Alcorn, R., 2013. Investigation to air
738   compressibility of oscillating water column wave energy converters. 32nd International
739   Conference on Ocean, Offshore and Arctic Engineering, Nantes, France, pp. V008T9A005.
740   https://doi.org/10.1115/OMAE2013-10151.

741   Sheng, W., Alcorn, R., Lewis, T., 2014. Physical modelling of wave energy converters. Ocean Eng.
742   84, 29-36. https://dx.doi.org/10.1016/j.oceaneng.2014.03.019.

743   Simonetti, I., Cappietti, L., Elsafti, H., Oumeraci, H., 2017. Optimization of the geometry and the
744   turbine induced damping for fixed detached and asymmetric OWC devices: A numerical study.
745   Energy 139, 1197-1209. https://doi.org/10.1016/j.energy.2017.08.033.

746   Simonetti, I., Cappietti, L., Elsafti, H., Oumeraci, H., 2018. Evaluation of air compressibility effects
747   on the performance of fixed OWC wave energy converters using CFD modelling. Renew.Energy
748   119, 741-753. https://doi.org/10.1016/j.renene.2017.12.027.

749   Stansby, P., Carpintero Moreno, E., Stallard, T., Maggi, A., 2015. Three-float broad-band resonant
750   line absorber with surge for wave energy conversion. Renew.Energy 78, 132-140.
751   https://doi.org/10.1016/j.renene.2014.12.057.

752   Taveira-Pinto, F., Iglesias, G., Rosa-Santos, P., Deng, Z.D., 2015. Preface to special topic: Marine
753   Renewable Energy. J.Renew.Sustain.Energy 7 (6), 061601. https://doi.org/10.1063/1.4939086.

754   Thakker, A., Hourigan, F., Dhanasekaran, T.S., El, H.M., Usmani, Z., Ryan, J., 2004. Design and
755   performance analysis of impulse turbine for a wave energy power plant. Int.J.Energy Res. 29 (1),
756   13-36. https://doi.org/doi.org/10.1002/er.1034.

757   Vanneste, D., Troch, P., 2015. 2D numerical simulation of large-scale physical model tests of wave
758   interaction with a rubble-mound breakwater. Coast.Eng. 103, 22-41.
759   https://doi.org/10.1016/j.coastaleng.2015.05.008.

760   Viviano, A., Naty, S., Foti, E., Bruce, T., Allsop, W., Vicinanza, D., 2016. Large-scale experiments
761   on the behaviour of a generalised Oscillating Water Column under random waves.
762   Renew.Energy
763   99, 875-887. https://doi.org/10.1016/j.renene.2016.07.067.

764   Vyzikas, T., Deshoulières, S., Barton, M., Giroux, O., Greaves, D., Simmonds, D., 2017.
765   Experimental investigation of different geometries of fixed oscillating water column devices.
766   Renew.Energy 104, 248-258. https://doi.org/10.1016/j.renene.2016.11.061.

767   Vyzikas, T., Deshoulières, S., Giroux, O., Barton, M., Greaves, D., 2017. Numerical study of fixed
768   Oscillating Water Column with RANS-type two-phase CFD model. Renew.Energy 102, 294-
769   305. https://doi.org/10.1016/j.renene.2016.10.044.

770   Weber, J., 2007. Representation of non-linear aero-thermodynamic effects during small scale physical
771   modelling of OWC WECs. 7th European Wave and Tidal Energy Conference, Porto, Portugal,
772   pp. 11-14.

773

Table 1

Table 1. Dimensions of the geometrical parameters of the OWC model.

Geometrical parameter	Symbol	Model dimensions
Chamber height	h_c	63.6 cm
Chamber length (in the wave direction)	l_c	12.8 cm
Chamber width (transverse to wave direction)	w_c	65.0 cm
Entrance height	h_e	12.8 cm
Vertical walls thickness	t_Z	2.0 cm
Horizontal walls thickness	t_X	2.8 cm
Orifice diameter	D	variable
Duct height	h_d	$25D$
Bedding height	h_b	8.0 cm
Bedding length	l_b	20.0 cm
Bedding slope	s	1:2

Table 2

Table 2. Wave conditions included in the numerical testing programme.

Wave condition	Model dimensions		Prototype dimensions	
	T	*H*	*T*	*H*
#1	1.20 s	0.06 m	6 s	1.5 m
#2	1.60 s	0.02 m	8 s	0.5 m
#3	1.60 s	0.04 m	8 s	1.0 m
#4	1.60 s	0.06 m	8 s	1.5 m
#5	1.60 s	0.08 m	8 s	2.0 m
#6	1.60 s	0.10 m	8 s	2.5 m
#7	2.00 s	0.06 m	10 s	1.5 m
#8	2.40 s	0.06 m	12 s	1.5 m
#9	2.80 s	0.06 m	14 s	1.5 m

Table 3

Table 3. Results of the numerical model validation based on the comparison between the experimental and numerical signals of pressure drop (Δp) and free surface elevation inside the OWC chamber (η_{OWC}).

D (mm)	Δp				η_{OWC}			
	R		**NRMSE**		**R**		**NRMSE**	
	average	*s*	*average*	*s*	*average*	*s*	*average*	*s*
28	0.9922	0.0044	0.0680	0.0186	0.9878	0.0044	0.0547	0.0131
31	0.9956	0.0073	0.0645	0.0204	0.9867	0.0050	0.0592	0.0117
39	0.9878	0.0097	0.0861	0.0316	0.9844	0.0113	0.0632	0.0159
	0.9919	**0.0079**	**0.0729**	**0.0252**	**0.9863**	**0.0074**	**0.0590**	**0.0136**

Table 4

Table 4. Results of the numerical model validation based on the comparison between the experimental and numerical signals of free surface elevation at two positions along the flume (η_{WG4} and η_{WG6}), for two different wave conditions.

| D (mm) | H = 0.02 m, T = 1.6 s | | | | H = 0.10 m, T = 1.6 s | | | |
| | η_{WG4} | | η_{WG6} | | η_{WG4} | | η_{WG6} | |
	R	NRMSE	*R*	NRMSE	*R*	NRMSE	*R*	NRMSE
28	0.9983	0.0635	0.9960	0.0379	0.9952	0.0816	0.9886	0.0806
31	0.9974	0.0665	0.9948	0.0443	0.9967	0.0859	0.9863	0.0835
39	0.9857	0.0718	0.9839	0.0708	0.9950	0.0823	0.9884	0.0776
	0.9938	**0.0673**	**0.9916**	**0.0510**	**0.9956**	**0.0833**	**0.9878**	**0.0806**

Table 5

Table 5. Inhalation, exhalation and representative values of the damping parameter (B) for the three orifice diameters tested.

D (mm)	B_{inh} (kg/m^7)		B_{exh} (kg/m^7)		B_r (kg/m^7)
	average	*s*	*average*	*s*	*average*
28	5.33×10^6	9.72×10^4	5.27×10^6	8.24×10^4	5.30×10^6
31	3.59×10^6	7.54×10^4	3.59×10^6	6.86×10^4	3.59×10^6
39	1.48×10^6	3.59×10^4	1.48×10^6	3.77×10^4	1.48×10^6

Table 6

Table 6. Global average values of the capture width ratio (C_{WR}) considering the whole set of wave conditions, for the three values of the damping coefficient.

B*	C_{WR}		Relative difference (%)
	incompressible set-up	compressible set-up	
160.49	0.278	0.250	−9.99
132.18	0.284	0.261	−8.08
84.85	0.256	0.265	+3.58

Figure 1

(A)

(B)

(C)

l_b

D

h_d

t_z

t_x

l_c

w_c

A

h_c

h_e

s

h_b

Section A-A

A
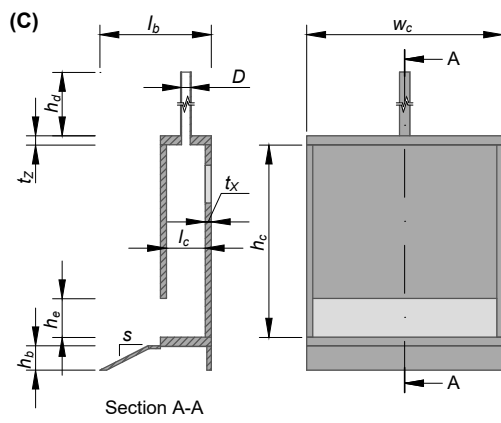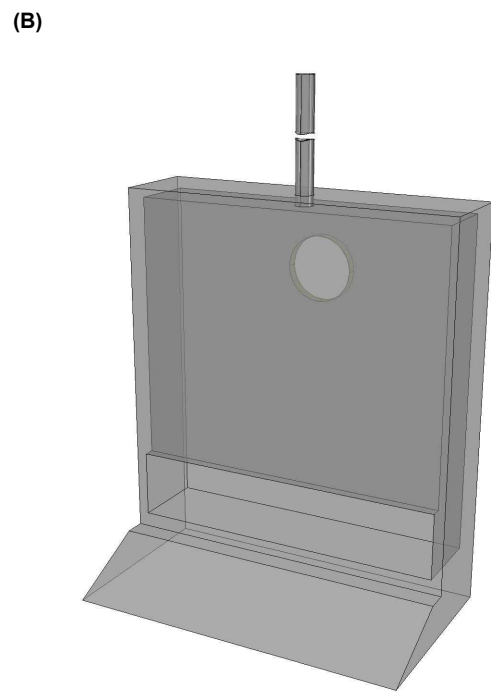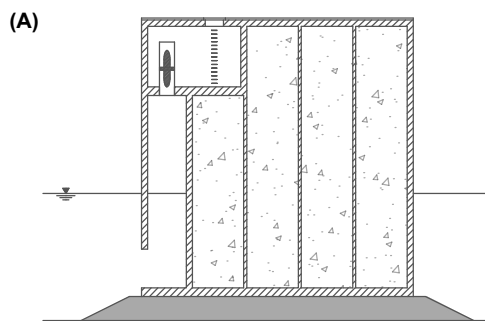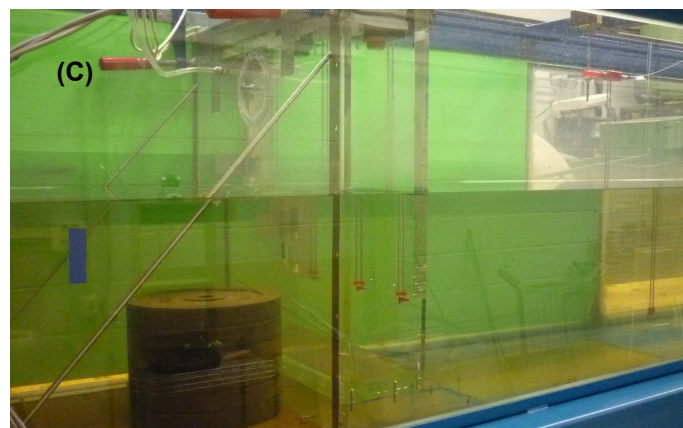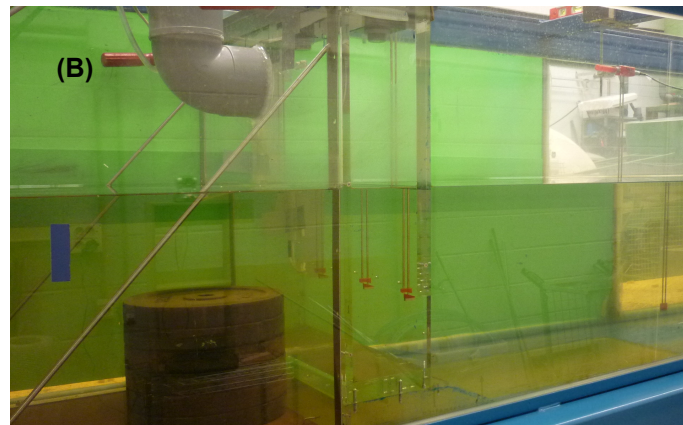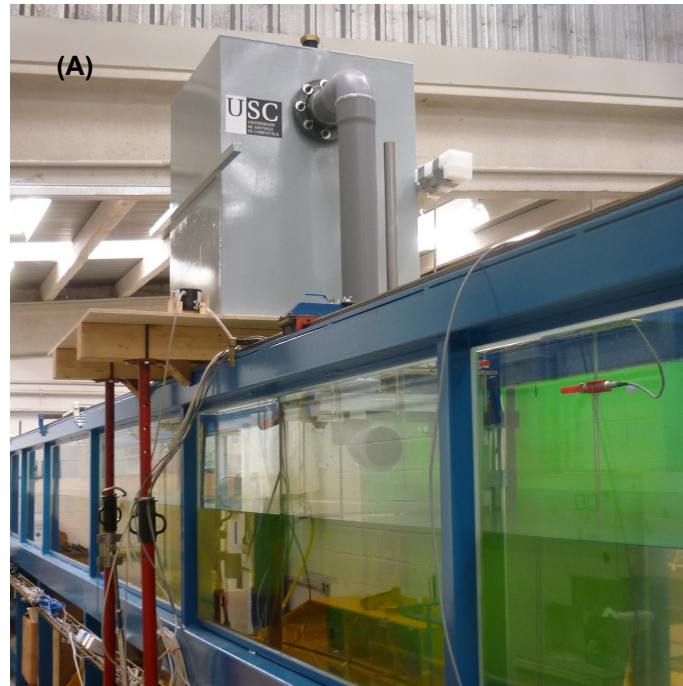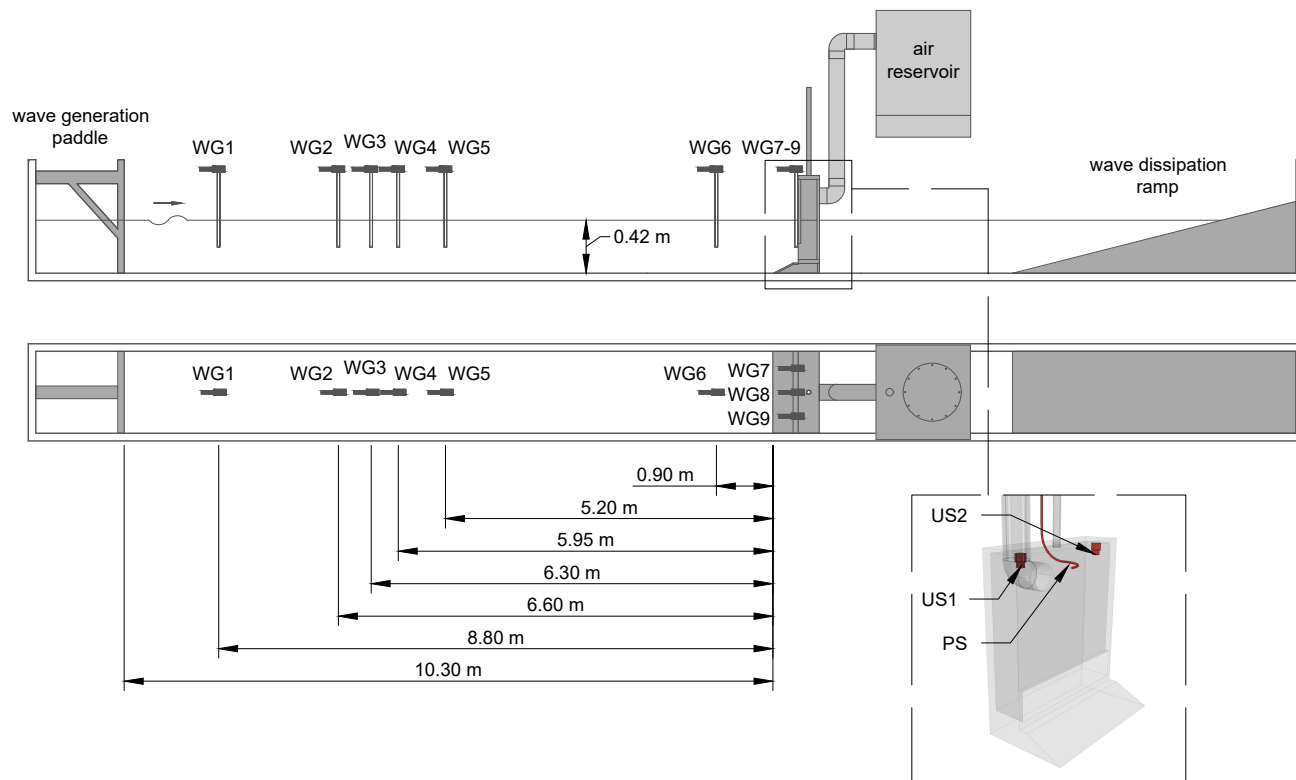
Figure 2

Figure 3

Figure 4
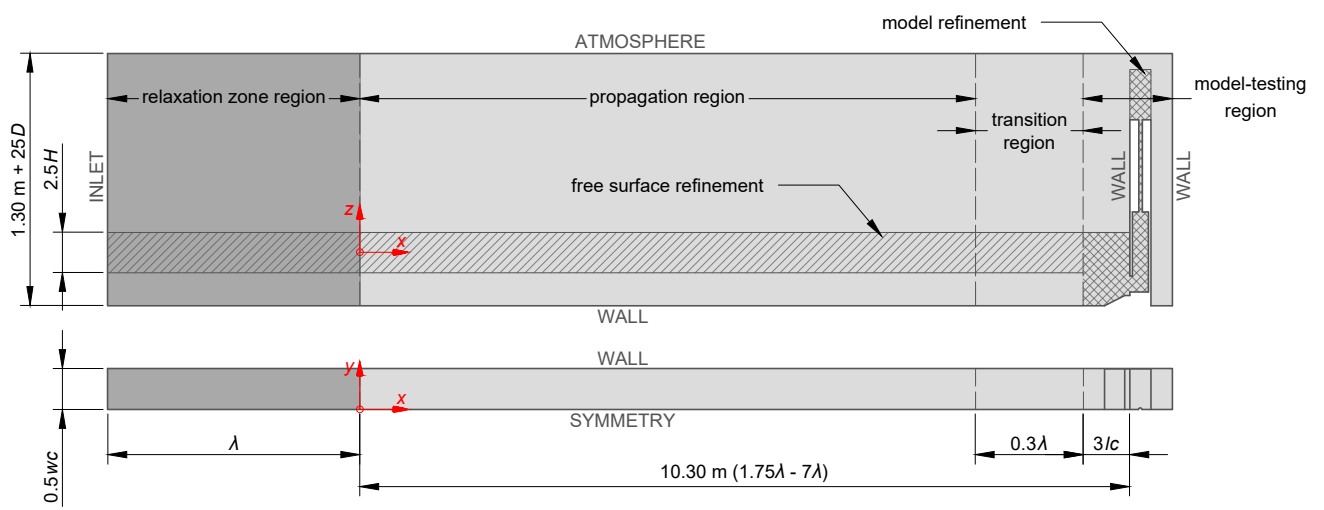
Figure 5
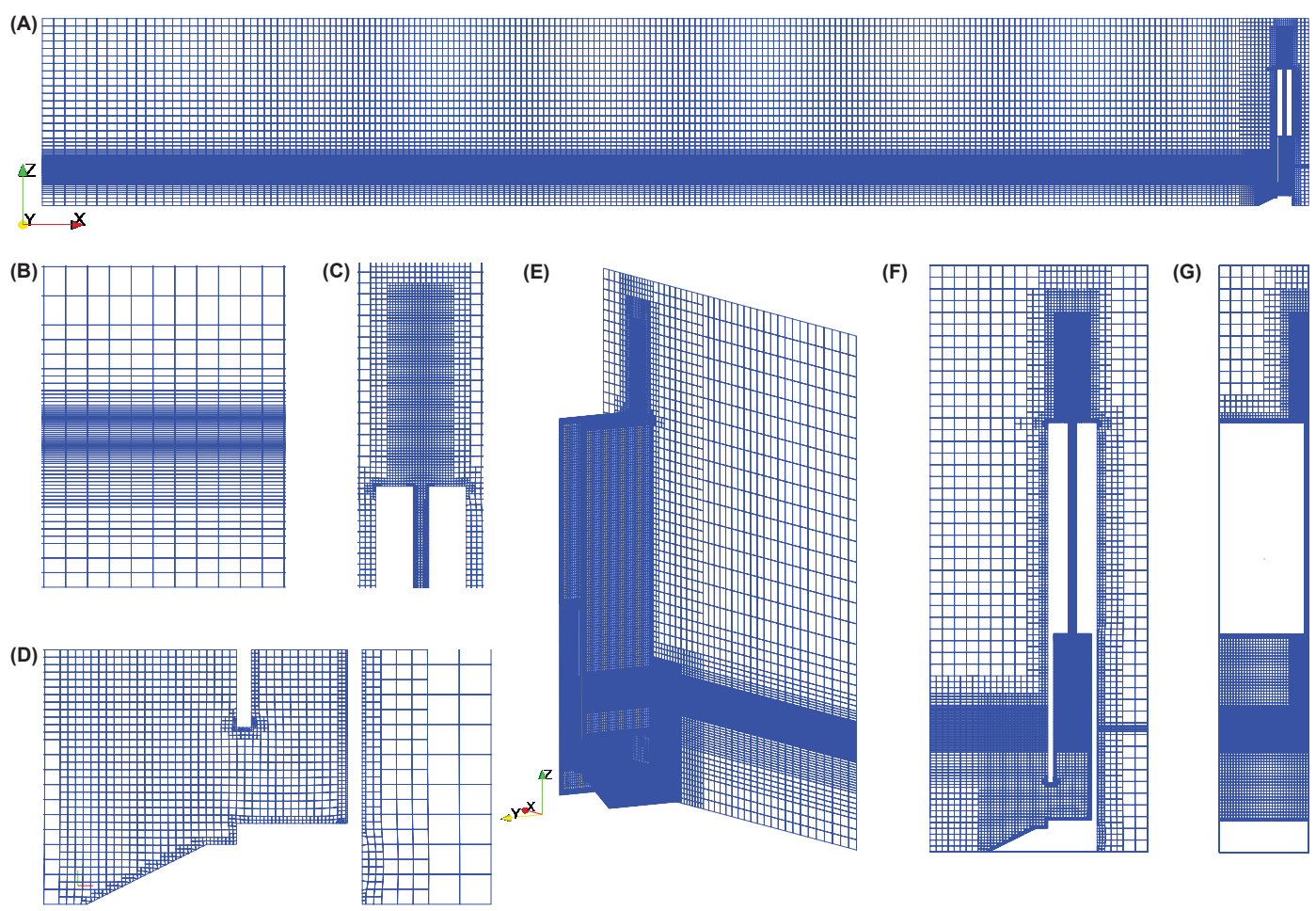
Figure 6
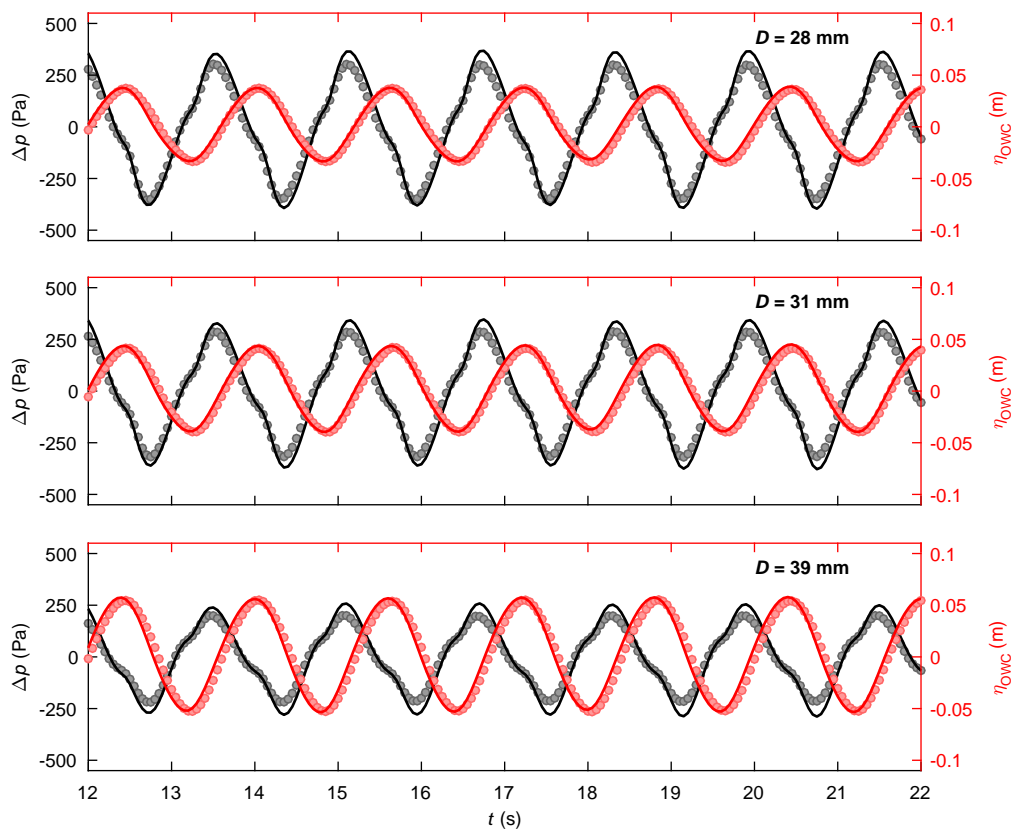
Figure 7
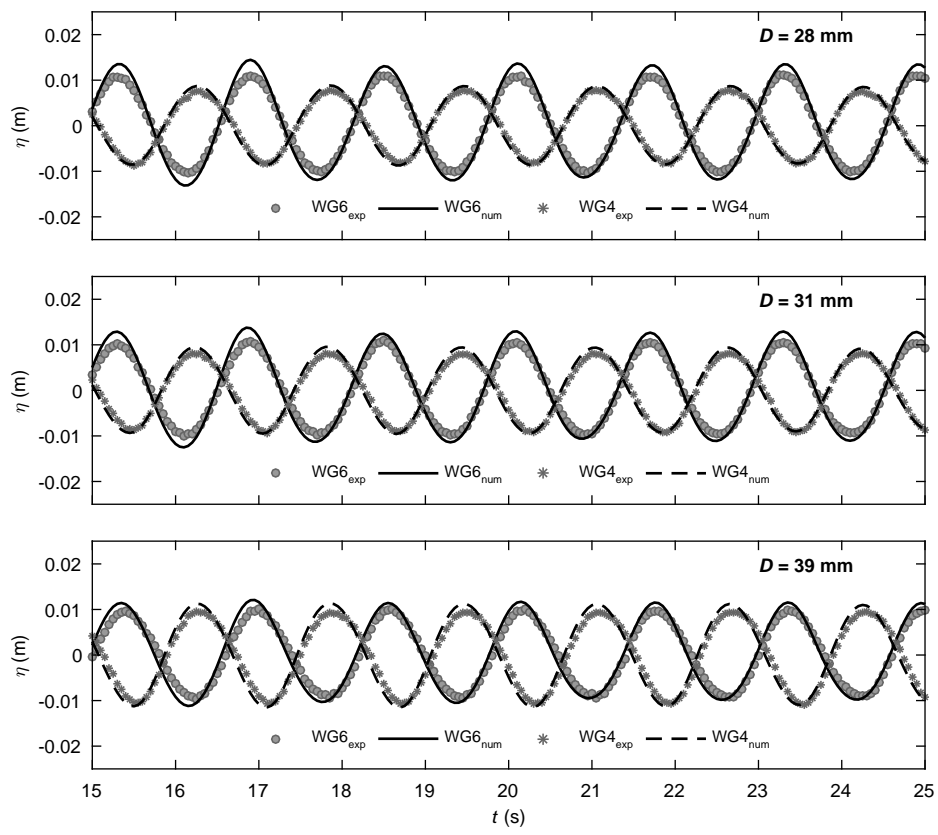
Figure 8

Figure 9

Figure 10